

Investigating the mass-ratio dependence of the prompt-collapse threshold with numerical-relativity simulations

Maximilian Kölsch¹, Tim Dietrich^{2,3}, Maximiliano Ujevic⁴, and Bernd Brügmann¹

¹*Theoretical Physics Institute, University of Jena, 07743 Jena, Germany*

²*Institut für Physik und Astronomie, Universität Potsdam,*

Haus 28, Karl-Liebknecht-Str. 24/25, 14476, Potsdam, Germany

³*Max Planck Institute for Gravitational Physics (Albert Einstein Institute),*

Am Mühlenberg 1, Potsdam 14476, Germany and

⁴*Centro de Ciências Naturais e Humanas, Universidade Federal do ABC, 09210-170, Santo André, São Paulo, Brazil*

(Dated: December 23, 2021)

The next observing runs of advanced gravitational-wave detectors will lead to a variety of binary neutron star detections and numerous possibilities for multi-messenger observations of binary neutron star systems. In this context a clear understanding of the merger process and the possibility of prompt black hole formation after merger is important, as the amount of ejected material strongly depends on the merger dynamics. These dynamics are primarily affected by the total mass of the binary, however, the mass ratio also influences the postmerger evolution. To determine the effect of the mass ratio, we investigate the parameter space around the prompt-collapse threshold with a new set of fully relativistic simulations. The simulations cover three equations of state and seven mass ratios in the range of $1.0 \leq q \leq 1.75$, with five to seven simulations of binary systems of different total mass in each case. The threshold mass is determined through an empirical relation based on the collapse-time, which allows us to investigate effects of the mass-ratio on the threshold mass and also on the properties of the remnant system. Furthermore, we model effects of mass ratio and equation of state on tidal parameters of threshold configurations.

I. INTRODUCTION

As proven by the combined multi-messenger observation of GW170817, AT2017gfo, and GRB170817A [1, 2], binary neutron star (BNS) mergers can be connected to a variety of observables in different observational channels, most notably, gravitational waves (GWs) and electromagnetic (EM) waves. However, not all BNS mergers will lead to a multi-messenger observation. In contrast to GW170817, the follow-up observations of GW190425 [3] did not reveal any EM signature connected to the detected GW signal. Such a non-detection could have multiple origins, e.g., the possibility that we observed GW190425 by an angle outside of the gamma ray burst (GRB) cone, or the possibility that (due to the poor localization) the correct sky location was not covered during the EM follow-up campaign. However, there is also the (very) likely scenario that the non-detection is related to the source parameters of GW190425; see e.g. [4, 5].

As discussed in Ref. [3], GW190425 had a total mass of $3.3_{-0.1}^{+0.1} M_{\odot}$ (low spin prior $|\chi| < 0.05$), this mass is noticeably larger than the estimated total mass of GW170817 [6] ($2.73_{-0.01}^{+0.04} M_{\odot}$) and the measured BNS masses in our galaxy. For such large masses, it is predicted that right after the merger of the two stars, the formed remnant collapses quickly to a black hole (BH). In most cases, such a *prompt-collapse* scenario does not lead to massive ejecta or a debris disk. Therefore, the potential kilonova [7–10] – an infrared, optical, ultraviolet transient triggered by the neutron-rich outflow material ejected during and after the merger – will be too dim to be detected. Similarly, if the debris disk is not massive enough, the energy that is stored within the

disk is not sufficient to successfully launch a GRB.

Over the last several years, numerous studies based on numerical-relativity (NR) simulations investigated under which circumstances a prompt-collapse scenario happens¹. In general, it was found that the threshold mass is k times larger than the maximum mass M_{\max} , supported by a non-rotating NS described by the Tolman-Oppenheimer-Volkoff equation:

$$M_{\text{thr}} = k M_{\max}. \quad (1)$$

One of the first studies that tried to determine k was presented by Hotokezaka et al. [12] in 2011 where a set of 6 EOSs has been studied and it was found that $k \in [1.3, 1, 7]$. Bauswein et al. [13] in 2013 also focused on equal mass and comparable mass ratio systems ($q = M_1/M_2 \lesssim 1.1$) for a set of 12 equations of state (EOSs) and derived a generic formula for the prompt-collapse threshold mass. This study was followed by Köppel et al. [14] who combined NR simulations and estimated free fall times to obtain upper bounds on the threshold mass. Agathos et al. [15] used another set of NR simulations and derived estimates that were based on the tidal deformabilities so that the inspiral GW signal could be connected directly to the measured GW signal.²

¹ For more details, we refer the interested reader to the review article of Bernuzzi [11].

² Agathos et al. [15] predict a 10% change that GW170817 led to a prompt-collapse, while GW190425 produced, with a probability of 96%, a BH right after merger [3].

Finally, Bauswein et al. [16] presented the first prompt-collapse study, in which a mass ratio dependent threshold (up to a mass ratio of $q \sim 1.4$) was derived. Very recently, Perego et al. [17] also investigated the effect of the mass-ratio on the prompt collapse threshold for non-spinning configurations. The spin-effect on the threshold mass has been investigated for the first time by Tootle et al. [18].

In this article, we will revisit the prompt-collapse threshold and its dependence on the employed EOS and the system's mass ratio. For this purpose, we present a large set of 290 new NR simulations with a mass ratio up to $q \leq 1.75$. While performing a systematic and detailed variation of the total mass and the mass ratio of the systems, we restrict our study to 3 EOSs, namely ALF2, SLy, and H4. For an investigation focusing on a larger set of EOSs, we refer the interested reader to [16].

Throughout the article we will employ geometric units and set $c = G = M_{\odot} = 1$, unless stated otherwise.

II. METHODS AND CONFIGURATIONS

A. Numerical Methods

1. Initial data construction

Our initial data (ID) are constructed with the SGRID code [19–23]. SGRID uses pseudospectral methods to solve the conformal thin sandwich equations [24–26]. In its newest form, SGRID [19] allows to study a large fraction of the BNS parameter space, including high spins, high masses, and mass ratios. This version employs an improved iterative solver and a larger number of computational domains (38 instead of originally 6 as in [21]) that are constructed such that star surfaces always coincide with (adaptable) domain boundaries. For the purpose of this work, SGRID got upgraded such that it allows to specify the individual components' masses of a BNS either as baryonic or gravitational mass. Previously, it was only possible to specify the baryonic mass. SGRID employs EOSs approximated by piecewise polytropes [19].

2. Dynamical evolutions

We use the BAM code for our dynamical evolutions. BAM solves the Einstein equations and the equations of general relativistic hydrodynamics (GRHD) on a domain of nested Cartesian grids. The evolution algorithm is based on the method of lines and an explicit Runge-Kutta time integrator is used. BAM utilizes adaptive mesh refinement (AMR) employing a Berger-Oliger scheme [27]. The metric variables are spatially discretized using finite difference stencils, while high resolution shock-capturing methods are applied to hydrodynamic variables [28–31].

We use the Z4c formulation of the 3+1 Einstein equations [32, 33] together with (1+log)-slicing for the

TABLE I. Grid configurations. As the number of levels is the same for all used resolutions, the names in the first column primarily refer to the number of grid points. However, the resolutions used for H4 are marked with a '*', as a different grid spacing was needed to fully cover the stars on the finest level. The numerical domain contains L grid levels of which L_{mv} are moving box levels. The number of grid points in each direction are n and n_{mv} respectively. The grid spacing on the finest level (innermost boxes covering the NSs), h_6 , is 2^6 times finer than the spacing on the coarsest level, h_0 . The last column refers to the outer boundary position R_0 .

Name	L	L_{mv}	n	n_{mv}	EOS	h_6 [m]	h_0 [km]	R_0 [km]
R3	7	4	320	160	ALF2, SLy	185	11.8	3781.1
R3*	7	4	320	160	H4	196	12.5	4008.0
R2	7	4	256	128	ALF2, SLy	231	14.8	3781.1
R2*	7	4	256	128	H4	245	15.7	4008.0
R1	7	4	192	96	ALF2, SLy	308	19.7	3781.1

lapse and gamma-driver conditions for the shift [34–36]. For the construction of the numerical fluxes of the GRHD system a local Lax-Friedrich (LLF) method is used. For the reconstruction of the primitive or characteristic variables a 5th order weighted-essentially-non-oscillatory (WENOZ) scheme [37] is employed. This high-order scheme is part of a hybrid algorithm described in Ref. [28]: In high density regions, we use a reconstruction of characteristic variables, while in low density regions the primitive variables are reconstructed.

Similarly to the construction of the initial data, we use piecewise-polytropic [38] representations of the zero-temperature EOSs SLy, ALF2 and H4. Since thermal effects can become important in the merger and post-merger phase of the BNS coalescence, we add a thermal pressure contribution given by $p_{th} = (\Gamma_{th} - 1)\rho\epsilon$, with an adiabatic constant of $\Gamma_{th} = 1.75$ [39, 40].

BAM uses a hierarchy of L nested refinement levels, with the lowest resolution being labeled by $l = 0$ and the finest resolution $l = L - 1$. Each level is characterized by a constant grid spacing h_l and the number of points n in each direction. The grid spacing at level l is given by $h_l = h_0/2^l$, h_0 being the grid spacing of level $l = 0$. The grid levels are nested such that each grid at level $l > 0$ is covered completely by a grid at level $l - 1$. The outermost grids with $l \leq l^{mv}$ are non-moving, while on levels with $l > l^{mv}$ there are moving boxes centered around the stars, i.e. simulating a BNS there are two non-overlapping grids or a single combined grid at levels with $l > l^{mv}$ [29]. Throughout this study we use $L = 7$ and $l^{mv} = 2$; see Tab. I for more details.

TABLE II. Sample of properties characterizing the EOSs studied in this work, ordered by stiffness. Columns from left to right: M_{\max} and R_{\max} are the gravitational mass and radius of the maximum-mass TOV star. $R_{1.4}$ and $R_{1.6}$ are the radii of single $1.4M_{\odot}$ and $1.6M_{\odot}$ TOV star respectively. $C_{\max} = (GM_{\max})/(c^2 R_{\max})$ is the compactness of the maximum-mass TOV configuration and $C_{1.6}^* = (GM_{\max})/(c^2 R_{1.6})$ an alternative formula for the compactness as given by Bauswein et al. in [13]. $\Lambda_{1.4}$ is the tidal deformability coefficient of a single $1.4M_{\odot}$ star.

EOS	M_{\max} [M_{\odot}]	R_{\max} [km]	$R_{1.6}$ [km]	$R_{1.4}$ [km]	C_{\max}	$C_{1.6}^*$	$\Lambda_{1.4}$	Ref.
SLy	2.06	9.91	11.46	11.37	0.307	0.268	306.7	[41]
ALF2	1.99	11.30	12.38	12.41	0.260	0.237	590.6	[42]
H4	2.03	11.62	13.54	13.46	0.258	0.223	885.6	[43]

B. Configurations

In this study, we consider a range of seven mass ratios

$$q = \frac{M_1}{M_2}, \quad M_1 > M_2, \quad (2)$$

conducting simulations for three EOSs and for each EOS individually adapted sets of the total binary masses M . For a given EOS the same total masses are investigated for all mass ratios.³ For all of these configurations we prepared ID containing irrotational stars at an initial separation of $16M_{\odot}$ (≈ 23.6 km) on quasi-circular orbits. We note that because of the short inspiral, we do not apply any additional eccentricity reduction procedure. The residual eccentricities are reasonably small (at the order of or below 10^{-2}), which we expect acceptable for the study that we plan to perform.

Table II summarizes important properties of the EOSs. Their maximum masses are $2.06M_{\odot}$, $1.99M_{\odot}$, and $2.03M_{\odot}$, respectively. Their predicted radii for a $1.4M_{\odot}$ NS are 11.46 km, 12.38 km, and 13.54 km. Hence, the chosen EOSs are broadly compatible with recent maximum mass and radius constraints, e.g., [44–54]⁴, but also cover a reasonably large range of compactnesses.

Within this work we will list the EOSs and related data with respect to the stiffness of the stars, from soft to stiff: SLy, ALF2, and H4, cf. Fig. 1, as results will

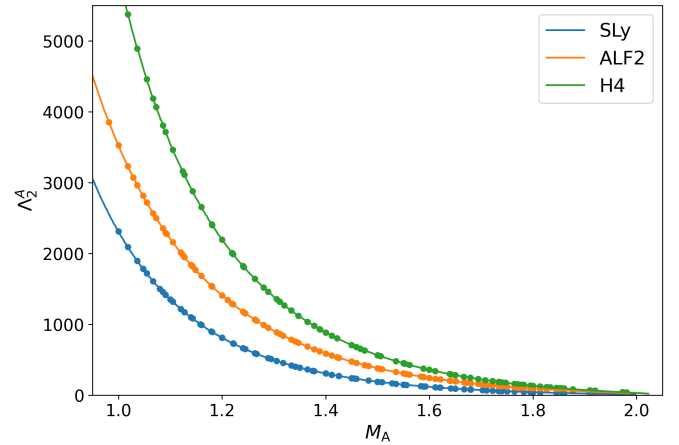


FIG. 1. Tidal polarizability coefficients Λ_2^A given as a function of the mass M_A of a single star A (solid lines). The tidal polarizability coefficients of configurations simulated for this study (data points) cover the range of about 15 to 5400. For a given mass M_A , SLy produces always the softest, H4 the stiffest star.

usually mirror this order. We refer to different quantities characterizing the tidal polarizability [Eqs.(3) to (5)] as a measure of the stiffness of the NS (cmp. [15]) For a single star A the tidal polarizability coefficient Λ_2^A is written as

$$\Lambda_2^A = \frac{2}{3} k_2^A \left(\frac{c^2 R_A}{G M_A} \right)^5, \quad (3)$$

where R_A and k_2^A are the radius and quadrupolar gravitoelectric Love number ([70–73]) of a single NS of gravitational mass M_A , respectively. The tidal polarizability coefficients of all binaries’ components simulated for this work are presented in Fig. 1. For BNSs we refer to the tidal polarizability parameters κ_2^T and $\tilde{\Lambda}$:

$$\kappa_2^T = \frac{3}{2} [\Lambda_2^A X_A^4 X_B + \Lambda_2^B X_B^4 X_A], \quad (4)$$

$$\tilde{\Lambda} = \frac{16}{13} \frac{(M_A + 12M_B)M_A^4}{M^5} \Lambda_2^A + (A \leftrightarrow B), \quad (5)$$

with $X_A = M_A/M$. Main properties of the simulated BNS configurations are given in Tabs. XI to XIII.

III. COLLAPSE TIME AND THRESHOLD MASS

A. Collapse Time

If the total mass of the system, for given mass ratio and EOS is high enough, its merger will result in the formation of a BH. We define the *collapse time* or remnant’s *life time* as the (coordinate) time interval between the time of merger, t_{mrg} , and the formation of a BH, t_{BH} :

$$t_{\text{coll}} = t_{\text{BH}} - t_{\text{mrg}}. \quad (6)$$

³ This rule is broken in a few cases of extreme mass ratios, where M_1 would exceed M_{\max} , and at low total masses for which no BH would be formed within reasonable simulation time.

⁴ Most recent multi-messenger constraints are constructed through perturbative quantum-chromodynamics computations, e.g. [55], massive radio pulsars observations [56–58], maximum mass constraint derived under the assumption that GW170817’s final remnant was a BH, e.g. [59–62], GW observations of BNSs [1, 3], kilonova and GRB afterglow measurements of GW170817 [2, 63, 64], X-ray measurements performed by the NICER [Neutron Star Interior Composition Explorer] [52, 65–67], and heavy-ion collision experiments [68, 69].

Different possible approaches to extract t_{mrg} and t_{BH} from simulation data have been described by Köppel et al. [14], e.g. using GWs, distance, apparent horizon formation or lapse for criteria. The criterion based on the minimum lapse function has recently been refined in the follow-up paper by Tootle et al. [18]. Here, we will identify the time of BH formation with the time of first discovery of an apparent horizon, t_{AH} , and the time of merger with the time of the first maximum in the GW strain amplitude⁵, t_{max} , i.e.,

$$t_{\text{coll}} = t_{\text{AH}} - t_{\text{max}}. \quad (7)$$

We note that throughout this article, we consider only the dominant 22-mode of the GW for the determination of t_{max} . This assumption seems valid since even for a mass ratio of $q = 1.75$ the energy emitted in the higher modes is $\lesssim 1\%$, cf. Fig. 16 of Ref. [74]. The described method of our choice and the refined method based on the minimum lapse function are illustrated in Figs. 2 and 3 in the top and middle panel, respectively. The examples show the neglectable differences of the order of 0.1ms in the results for the collapse time that we typically find comparing the two methods.

B. Threshold Mass to Prompt Collapse

In this section, we review definitions of the threshold mass to prompt collapse, criteria for prompt and delayed collapse, and approaches to determine the threshold mass.

A basic definition of the threshold mass has been given by Bauswein et al. in [13], where the threshold mass M_{thr} separates the two scenarios of prompt and delayed collapse, i.e., the threshold mass is the lowest total mass M for which the merger product collapses to a BH promptly after merger. This definition naturally leads to the discussion, when a merger process resulting in the formation of a BH is to be considered *prompt*. While the semantics of the term *prompt* seem to ask for the discussion of a timescale, criteria found in the literature are based on different quantities.

Refs. [11, 12] define a prompt collapse through the behaviour of the density, i.e., when there is no bounce following the cores' collision and the central density increases monotonically until BH formation (cmp. bottom panel in Fig. 2 opposed to Fig. 3). Similarly, one can also consider the minimum of the lapse α_{min} instead of the central density of the remnant. Equivalently to the case of the maximum density, the criterion for prompt collapse

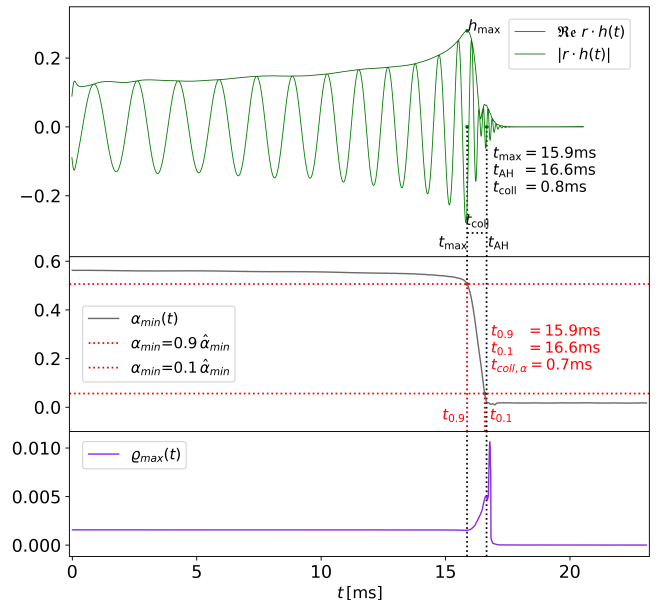


FIG. 2. Example of a prompt-collapse merger (EOS: SLy, $q = 1.125$, $M = 2.9 M_{\odot}$). Top panel: 22-mode, rh_{22} , of the GW (shifted according to an observer distance of 1477 km), where h_{22} refers to the 22-mode strain amplitude. Marked are the time maximum, t_{max} , and the time, t_{AH} when an apparent horizon was first found. Middle Panel: The minimum lapse function, $\alpha_{\text{min}}(t)$, falls monotonously. Marked are the points where $\alpha_{\text{min}}(t)$ has fallen to 90% and 10% of its maximum value. Bottom panel: The maximum density function, ρ_{max} , increases after merger without oscillations before it reaches a peak around the time a BH forms. The top and middle panel illustrate methods to determine the collapse time.

considering the minimum lapse function is a monotonous decrease of α_{min} [16], cf. middle panel in Fig. 2. In the case of a delayed collapse, on the other hand, the merger is followed by oscillations of the maximum-density and the minimum-lapse function, cmp. middle panel in Fig. 3. Considering, for completeness, the case of long-lived remnants with no collapse to BH during simulation time (cmp. Fig. 4), the maximum density and minimum lapse stabilize after an interval of oscillations. Applying either one of the density or the lapse criteria to a set of simulation data, the threshold mass is typically localized by a bracketing method, cmp. for example [12, 13, 18].

A different approach has been taken by Köppel et al. [14], who base their threshold-mass definition directly on the free-fall time τ_{ff} , stating that the merger remnant of a configuration with $M = M_{\text{thr}}$ would collapse over a timescale given by the collapse time of a maximum-mass configuration. However, we note that typical free-fall times of about 0.1 ms are noticeably smaller than the smallest collapse times found in our simulations. In the framework, described in [14], the threshold mass is calculated using an extrapolation of an exponential fit based on a small number of simulations. Comparing threshold

⁵ The strain amplitude h being a function of the retarded time, $u = t - r_*$, where r_* depends on extraction radius, r_{extr} . (Cmp. [74]) We will not explicitly use this denomination, i.e., $h(t)$ will be the shifted waveform (cmp. Figs. 2 to 4), t_{max} will denote the shifted time of maximum.

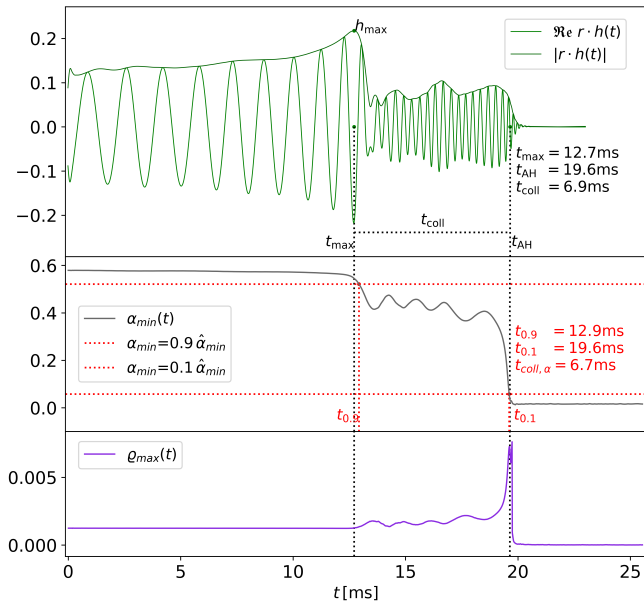


FIG. 3. Example of a delayed collapse (EOS: H4, $q = 1.375$, $M = 2.95 M_{\odot}$) compared to the prompt-collapse case presented in Fig. 2 there is a richer postmerger signal which drops down to zero at a later time after merger. The maximum density function and the minimum lapse function are oscillating between merger and collapse.

masses reported in Refs. [14] and [16], we find only small differences in the results of these different approaches.

In this work, we will follow a new path to determine M_{thr} . This contains a package of three ingredients, which we will discuss in the following. Like Köppel et al. [14], we will perform a fit of collapse-time data. Yet, we will consider a different time-scale and a broad mass-interval, intending to localize M_{thr} by means of interpolation. The timescale associated with the threshold to prompt collapse will be motivated in the following. A detailed discussion of the fitting procedure follows in Sec. IV C.

As found by Bauswein et al. [13], the precise identification of M_{thr} [based on a bracketing method] is problematic, as the collapse time has a steep sensitivity to the total mass M in the vicinity of M_{thr} ⁶. However, while the collapse time is sensitive to small changes in M for $M \sim M_{\text{thr}}$, the reverse relation is true for M as a function of t_{coll} . Therefore, within a certain tolerance, the threshold mass can be assigned a fix value of t_{coll} , which afterwards can be used to determine M_{thr} through interpolation. Investigating our set of 290 simulations with respect to the density and lapse criteria, we find that independent of the resolution and the EOS, systems perform a prompt collapse for $t_{\text{coll}} \lesssim 2$ ms. For all simulations with $t_{\text{coll}} \gtrsim 2$ ms on the other hand, we find

⁶ An example of a collapse-time curve, finely resolved for $M \sim M_{\text{thr}}$, is presented in Sec. V.

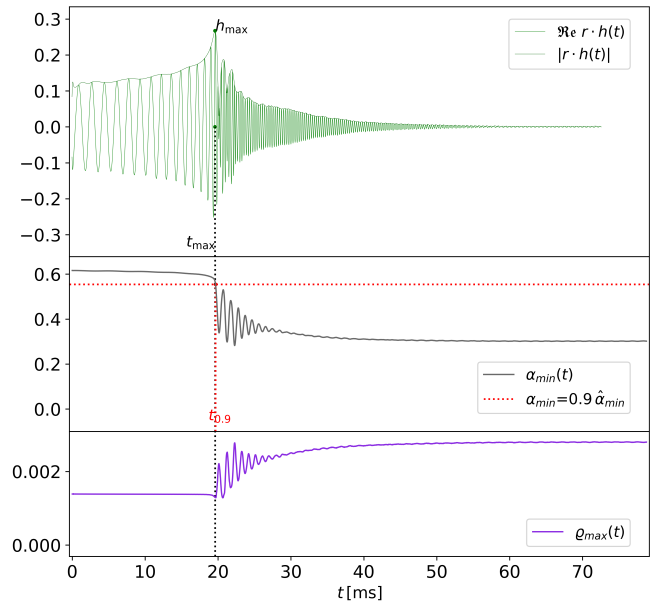


FIG. 4. Example of a long-lived remnant NS (EOS: SLy, $q = 1.0$, $M = 2.7 M_{\odot}$). The postmerger GW signal decreases in amplitude over a period of approximately 30 ms. The minimum lapse function and the maximum density function stabilize after an interval of oscillations following the merger.

oscillations in the maximum-density and minimum-lapse function in the interval between merger and collapse. We suggest to use this timescale to define the threshold to prompt collapse by means of a *threshold collapse time*

$$\tau_{\text{thr}} = 2 \text{ ms} . \quad (8)$$

Following this thought, we will call a collapse prompt (delayed) if the collapse time is smaller (larger) than 2 ms, and define the threshold mass as the total binary mass that corresponds to a collapse time that equals τ_{thr} . We point out that the choice for 2 ms as a threshold in the collapse time has also been made by Agathos et al., cf. [15].

Identifying the lifetime of a BNS merger remnant with the collapse time, Eq. (6), and extending the classification given in [12], we consider four types of mergers: prompt-collapse mergers (type I), delayed-collapse mergers (type II, III), and stable remnants with no collapse within simulation time, (type IV). Distinguishing between short-lived hypermassive neutron star (HMNS) and long-lived remnants, based on the time interval between t_{max} and t_{AH} , we build upon the classification by Hotokezaka et al. [12].

- Type I: prompt collapse ($t_{\text{coll}} < \tau_{\text{thr}}$)
- Type II: short-lived HMNS ($\tau_{\text{thr}} < t_{\text{coll}} < 5$ ms)
- Type III: long-lived remnants ($t_{\text{coll}} > 5$ ms)
- Type IV: long-lived remnants (no collapse within simulation time)

Note the usage of the threshold collapse time, τ_{thr} , in the definition of types I and II.

C. Threshold Mass Coefficient k_{thr}

It is common practice (c.f., for example, [12–14, 75]) to relate the threshold mass to the maximum mass M_{max} of an isolated, non-rotating NS predicted by the respective EOS in terms of a linear relation

$$M_{\text{thr}} = k_{\text{thr}}(\text{EOS}) \cdot M_{\text{max}}, \quad (9)$$

where M_{thr} , k_{thr} , and M_{max} depend on the EOS. In simulations of non-spinning equal mass BNSs with different EOSs the coefficient k_{thr} has been found in the range

$$1.3 \lesssim k_{\text{thr}} \lesssim 1.7, \quad (10)$$

(cmp. [12, 13, 15, 76]). Our results for k_{thr} (cmp. Tab. IV) agree with this inequality. The effect of the mass ratio q on this factor, i.e.,

$$M_{\text{thr}}(q) = k_{\text{thr}}(q) \cdot M_{\text{max}}. \quad (11)$$

will be discuss in Sec. IV D.

IV. DATA ANALYSIS AND RESULTS

A. Collapse types

As introduced in Sec. II B, the parameter space is defined by seven mass ratios and three EOSs. For each EOS an adapted set of total masses has been studied. The mass intervals are intended to contain both prompt and delayed-collapse mergers. Configurations that do not lead to a collapse during simulation time (hereafter referred to as *stable*) are of lesser importance to this study. Due to different properties of the respective EOSs the mass intervals do not coincide: Going from SLy, over ALF2, to H4, the transition from stable-remnant scenarios to collapse scenarios (depending on the mass ratio) is located at increasing total masses.

In Tab. III we present results in terms of collapse types, as introduced in Sec. III B. In addition, Tab. III gives a representation of the parameter space studied in this work. For high mass ratios the more massive component of the binary, M_1 , would exceed the maximum mass of a TOV star, i.e., $M_1 > M_{\text{max}}$. Hence, going to higher total masses the limits of the parameter space are met earlier for high mass ratios, and the cells in the lower-right corner stay empty.

For each EOS, going towards smaller total masses, the investigated parameter space contains simulations of type IV, i.e., no BH was formed within the simulation time. Therefore, to save computational resources, the respective total masses have not been investigated for all mass ratios. Usually, configurations have been simulated for

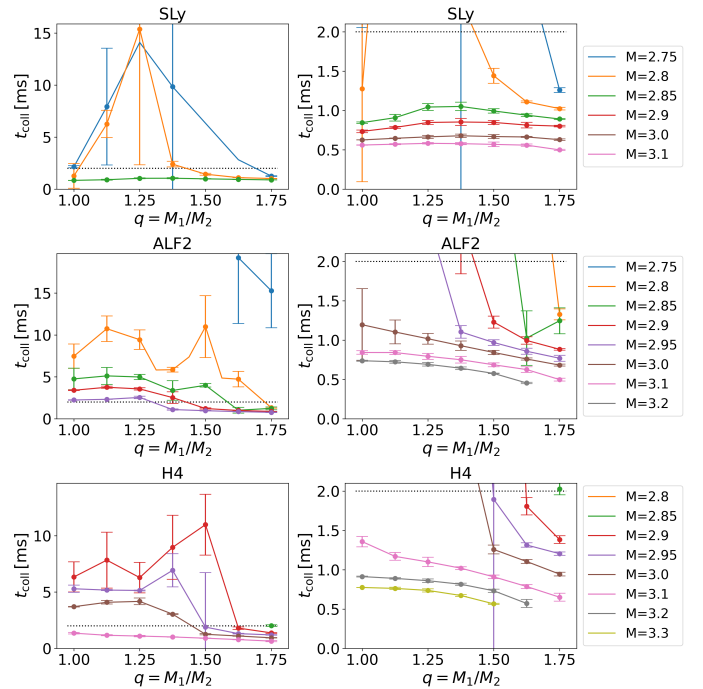


FIG. 5. Collapse time t_{coll} as a function of the mass ratio q for different total masses M . Rows: Data subsets defined by the EOS. The curves either decrease for increasing M or show a maximum for $q > 1$. For fixed mass ratio, t_{coll} decreases when we increase the total mass M . Left column: Full range of t_{coll} . Right column: Small collapse times.

more than one numerical resolution to obtain error estimates (cmp. Tab. I for details on the resolutions used). For most configurations the collapse types match within the set of simulated resolutions. However, there may be deviations. The biggest differences, with respect to the lifetime of the merger product, are usually found at the lower end of the investigated mass intervals, e.g., merger remnants of a given configuration may be short-lived for one resolution and long-lived for another resolution (e.g. ALF2 with $M = 2.8 M_{\odot}$), or long-lived for both resolutions, where a BH is only formed in one of the cases (e.g. SLy with $M = 2.75 M_{\odot}$). While there are deviations for low masses, the differences between results from different resolutions are small in the regime of higher masses, cf. also Figs. 5 and 6.

B. Mass Ratio Effects on t_{coll}

The collapse time t_{coll} naturally depends on the total mass M . The higher M the smaller t_{coll} , but apart from the total mass M , also other properties of the binary, such as the mass ratio q , affect the collapse time. This is illustrated in Fig. 5, where we plot $t_{\text{coll}}(q)$ for fixed values of M . Total masses that lead to high collapse times are presented on the left, while plots on the right focus on the prompt-collapse cases.

TABLE III. Summary of simulations and collapse types: Columns are ordered by increasing total mass of the binaries, rows are ordered by increasing mass ratio and subdivided by the EOSs. The collapse types (cmp. section III B) may differ between resolutions. In these cases, all types are given with reference to their respective resolution. In cases where a configuration has only been simulated with one resolution, the respective resolution is given as an index.

q	M		2.7	2.75	2.8	2.85	2.9	2.95	3.0	3.1	3.2	3.3
	EOS											
1.0	SLy		IV_{R3}	II	I_{R3}/II_{R2}	I	I	I	I	I		
	ALF2				III	II_{R3}/III_{R2}	II	II	$I_{R3}/I_{R2}/II_{R1}$	I	I	
	H4				III_{R2*}		III	III_{R3*}/II_{R2*}	II	I	I	I
1.125	SLy			III	III_{R3}/II_{R2}	I	I	I	I	I		
	ALF2				III	III	II	II	I	I	I	
	H4					III	III	III	II	I	I	I
1.25	SLy		IV_{R3}	III_{R3}/IV_{R2}	III_{R3}/II_{R2}	I	I	I	I	I		
	ALF2				III	II	II	II	I	I	I	
	H4					III	III	III	II	I	I	I
1.375	SLy			III	II	I	I	I	I	I		
	ALF2				III	II	II	I	I	I	I	
	H4					III	III	III	II	I	I	I
1.5	SLy		IV_{R3}	IV_{R3}/III_{R2}	I	I	I	I	I	I		
	ALF2				III	II	I	I	I	I	I	
	H4					III	III	I_{R3*}/III_{R2*}	I	I	I	I
1.625	SLy			II_{R3}/IV_{R2}	I	I	I	I	I	I		
	ALF2		IV_{R3}	III	II_{R3}/III_{R2}	I	I	I	I	I	I	
	H4				IV_{R2*}	IV_{R3*}/III_{R2*}	I	I	I	I	I	
1.75	SLy		IV_{R3}	I	I	I	I	I	I	I		
	ALF2		IV	III	I	I	I	I	I	I		
	H4				IV_{R2*}	II_{R3*}/I_{R2*}	I	I	I	I		

The error bars given in the plot are estimates, calculated as the difference between results from the highest resolution (R3 or R3*) and the medium resolution (R2 or R2*). Error bars are plotted symmetrically about the data points of highest resolution. For high total masses, error bars are squeezed together tightly due to small deviations between resolutions. Data underlying Fig. 5 are also given in the appendix (Tabs. XIV to XVI). As visualized in Fig. 5, (for a given total mass M) the collapse time t_{coll} becomes less systematic along the mass ratio interval, the longer the remnant NS survives. This is the case for lower masses, where t_{coll} as a function of q typically has at least one maximum for $q > 1$. For high masses t_{coll} is almost linear in q . At the upper end of investigated mass ratio interval (for fixed M) the collapse time is typically a decreasing function in q .

C. Localization of M_{thr}

One way to localize M_{thr} for given EOS and mass ratio, is to narrow down the interval between the lowest total mass, $M_{\text{lower}}^{\text{prompt}}$, leading to prompt collapse, and the highest total mass, $M_{\text{upper}}^{\text{delayed}}$, for which the collapse is delayed. This bracketing method localizes the threshold mass within the interval

$$M_{\text{upper}}^{\text{delayed}} \leq M_{\text{thr}} < M_{\text{lower}}^{\text{prompt}}. \quad (12)$$

In this approach, the threshold mass is defined as the mean value, $M_{\text{thr}} = 0.5(M_{\text{lower}} + M_{\text{upper}})$, cf. e.g. [13, 77].

In this chapter, we propose a method to determine M_{thr} based on a fitting procedure and the definition of a threshold collapse time τ_{thr} , introduced in Sec. III B. We use a fit of the collapse time to determine M_{thr} as the value of M , where

$$t_{\text{coll}}(M) = \tau_{\text{thr}}, \quad (13)$$

is satisfied. The fit function is empirically motivated and constructed such that the following criteria are met. These criteria are assumptions about the asymptotic behaviour of t_{coll} and observations about the simulated data:

1. At lower total masses we assume the maximum mass $M_{\text{max}}^{\text{rot}}$ of rigid rotation⁷ to mark the threshold to stable remnant NS configurations ($t_{\text{coll}} \rightarrow \infty$). The collapse time (lifetime) therefore has to increase strongly for $M \rightarrow M_{\text{max}}^{\text{rot}}$ ⁸.
2. The time between merger and BH formation, t_{coll} , decreases for increasing M . Asymptotically, the

⁷ The maximum masses $M_{\text{max}}^{\text{rot}}$ of rigid rotation of the EOS studied in this work are 2.507342 M_{\odot} for SLy, 2.510254 M_{\odot} for ALF2, and 2.476984 M_{\odot} for H4; cf. [78].

⁸ We mention that possibly even higher masses than $M_{\text{max}}^{\text{rot}}$ could have been used as upper bound, since part of the total mass/energy will be released through ejecta and GW emission, e.g., [79–81].

function describing the relation has to approach a minimal value⁹, though of course the allowed range of total masses is finite.¹⁰ As an argument for the existence of a lower bound to the collapse time, the free-fall-time of a maximum mass TOV star of the respective EOS can be put forward (cmp. discussion in [14]).

- Equivalently to the condition described by equation (12), which may be based on any suitable criterion distinguishing between prompt and delayed collapse, we assume the threshold mass to lie between the two data points marking the highest mass with $t_{\text{coll}} > \tau_{\text{thr}}$ and the lowest mass with $t_{\text{coll}} < \tau_{\text{thr}}$.¹¹

We use a function which automatically satisfies the first and second assumption:

$$t_{\text{coll}}(M) = (\tau_{\text{thr}} - c) \exp \left[-a \frac{M - b}{M - M_s} \right] + c. \quad (14)$$

The primary building block of the fit function (14) is an exponential function with negative exponent. This is in accordance with our assumptions regarding the asymptotic behaviour. The function provides three fit-parameters (a, b, c) and one external parameter (M_s), which we set to the EOS-dependent maximum mass of a rigidly rotating NS, $M_s = M_{\text{max}}^{\text{rot}}$. It is build into the fit function such that it has a pole, $t_{\text{coll}} \rightarrow \infty$, at $M \rightarrow M_s$. The function provides a lower bound ($c > 0$) to the collapse time (even beyond the range of eligible values of M).

As implied by condition (13), we demand Eq. (14) to satisfy $t_{\text{coll}}(M_{\text{thr}}) = \tau_{\text{thr}}$. Therefore the parameter b equals the threshold mass M_{thr} , i.e.,

$$b = M_{\text{thr}}. \quad (15)$$

This construction has two advantages. First, we do not need to invert the fit formula to determine the threshold mass and its error, as it would be the case for a generic fit formula. In this setup, we simply take the error Δb , as determined by the least squares routine, for the error ΔM_{thr} of M_{thr} . Secondly, the application of bounds to the parameter b allows for a restriction of M_{thr} , to enforce implications of the third assumption.¹²

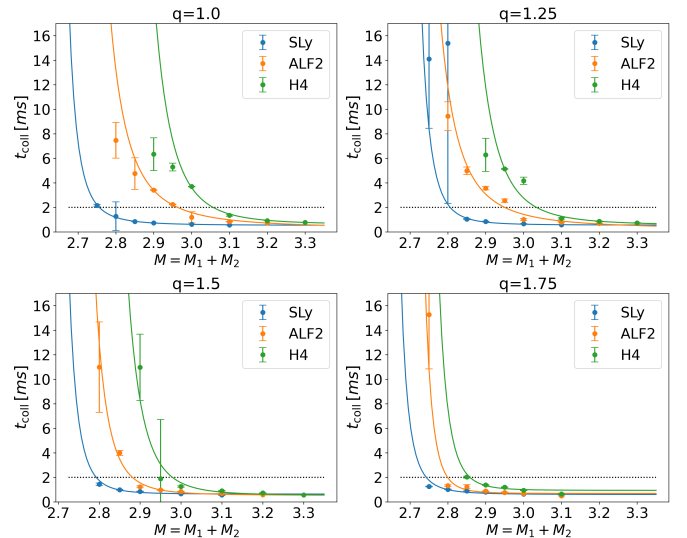


FIG. 6. Collapse time t_{coll} as a function of the total mass M for a sample of four mass ratios. For each EOS, the data are fitted based on Eq. (14). SLy, ALF2, and H4 are presented in blue, orange, and green respectively. The collapse time increases strongly for decreasing M and levels off for increasing M . The horizontal line at $t_{\text{coll}} = \tau_{\text{thr}} = 2$ ms marks the threshold to prompt collapse. The total mass corresponding to this intersection, M_{thr} , increases with higher tidal deformability.

To determine M_{thr} for given EOS and q by means of a least squares approach, we apply the fit function (14) to each subset of collapse time data, specified by EOS and mass ratio, taking into account data of configurations (EOS, q , M) that lead to BH formation in their highest resolution, i.e., R3 in the case of SLy and ALF2, R3* in the case of H4.

In cases where the data set does not provide data points (M , t_{coll}), with $t_{\text{coll}} > \tau_{\text{thr}}$ (for example SLy for $q = 1.5$, cmp. Fig. 6), without further assumptions, the parameters a and b become weakly determined. A similar obstacle arises due to large error-bars on collapse times at the lower end of the mass interval (for example SLy for $q = 1.25$, cmp. Fig. 6). These data points become virtually invisible to the fitting procedure. Therefore, when applying the least-squares algorithm, we add penalty terms to the fit function, demanding the fit function to reach a minimum value at low masses. In the case of large error-bars the fit is enforced to reach the lower end of the left-most errorbar. In the case of absent type-II or type-III data points in a subset of data, fit is enforced to reach the highest collapse time, found over all R3 simulations, at masses for which either no BH was formed, or no BH is expected to form within the simulation time. To give an example, for the EOSs SLy and ALF2 no BH formed within simulation time in the case of configurations with $M = 2.7 M_{\odot}$.

In cases where data points with collapse times above τ_{thr} are available, this procedure has no noticeable effect.

⁹ While the described asymptotic behavior can be observed within the data set, cf. Fig. 6, further investigations are needed for low mass ratios.

¹⁰ For high total masses M , the parameter space is limited by the allowed range of the mass M_1 of the more massive component, i.e., $M_1 < M_{\text{max}}$.

¹¹ If the condition $t_{\text{coll}} > \tau_{\text{thr}}$ is not met for any data point within a data subset defined by a parameter pair (q , EOS), then $M_{\text{upper}}^{\text{delayed}}$ is instead set to the total mass M for which we do not expect BH formation.

¹² In cases characterized by $|t_{\text{coll}} - \tau_{\text{thr}}| < \varepsilon$, these bounds on the parameter b are weakened, accounting for uncertainties on single data points (cmp. H4 fit for the $q = 1.5$ case in Fig. 6).

In the complementary case, this procedure balances the overweight of data points with collapse times below τ_{thr} . A sample of data and fits are presented in Fig. 6.

D. Mass Ratio Effects on M_{thr} and k

In this section, we will focus on the discussion of the threshold mass data (M_{thr} and k) and compare our data to results of Bauswein et al. [16], who have conducted BNS simulation for a large sample of 40 EOS to study the effect of mass ratio on the threshold to prompt collapse. Tab. IV summarizes quantities at the threshold to prompt collapse, i.e., M_{thr} , k , κ_2^{T} , and $\tilde{\Lambda}$. The behaviour of the tidal deformability quantities (κ_2^{T} and $\tilde{\Lambda}$) at the threshold to prompt collapse will be discussed in Sec. IV E.

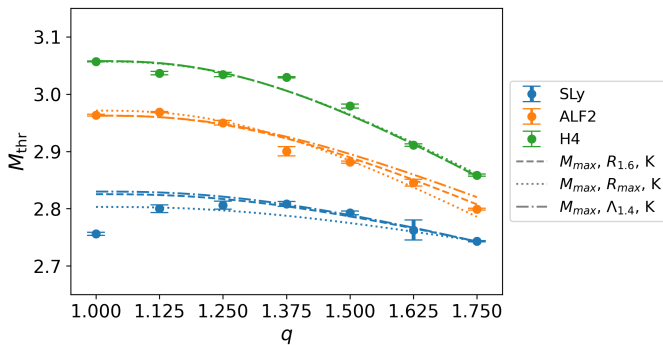


FIG. 7. Data points: threshold mass M_{thr} , as determined in this work, plotted as a function of the mass ratio q . M_{thr} decreases for increasing q . In the SLy case the curve possesses a clear maximum at $q \approx 1.375$. Dashed/dotted lines: Fits to the data points, for different stellar parameters, as given in the legend, based on the fit formula proposed by Bauswein et al. in [16] [reproduced in Eq. (16)]. The respective coefficients are given in Tab. VIII.

Based on the three EOSs and seven mass ratios, we obtain 21 data points for the threshold mass as a function of q . Fig. 7 shows these results for M_{thr} together with fits to the data based on a least squares approach and a fit formulae proposed by Bauswein et al. [16] (the respective coefficients c_1 to c_5 are given in Tab. VIII). They discussed fit formulae of the type $M_{\text{thr}} = \alpha(1 - q)^n + \gamma$, finding $n = 3$ to be the best compromise to describe all of their data. Based upon this observation they condense their findings into a set of general q -dependent fit formulae based on data for $\tilde{q} \in \{0.7, 0.85, 1.0\}$ and different pairs of independent stellar parameters (X, Y) characterizing the EOSs:

$$M_{\text{thr}}(q, X, Y) = c_1 X + c_2 Y + c_3 + c_4 \delta\tilde{q}^3 X + c_5 \delta\tilde{q}^3 Y, \quad (16)$$

with $\delta\tilde{q} = 1 - \tilde{q}$. Note the inverse definition of the mass ratio $\tilde{q} = 1/q < 1$ compared to the one used in our work.

With respect to results for ALF2 and H4, up to high mass ratios, our data points can be described well by the

TABLE IV. Quantities at the threshold to prompt collapse for all 21 cases (EOS, q). Presented in columns 3-10 are the threshold mass M_{thr} , the threshold mass coefficient k_{thr} , the tidal polarizability parameter κ_2^{T} and the tidal polarizability coefficient $\tilde{\Lambda}$ at threshold, and their respective errors.

EOS	q	M_{thr} [M_{\odot}]	ΔM_{thr} [M_{\odot}]	k_{thr}	Δk_{thr}	κ_2^{T}	$\Delta \kappa_2^{\text{T}}$	$\tilde{\Lambda}$	$\Delta \tilde{\Lambda}$
SLy	1.000	2.756	0.003	1.338	0.001	31.9	0.9	341	17
SLy	1.125	2.800	0.007	1.359	0.003	29.2	2.2	311	42
SLy	1.250	2.806	0.007	1.362	0.003	30.0	2.1	319	41
SLy	1.375	2.808	0.004	1.363	0.002	31.6	1.5	334	28
SLy	1.500	2.793	0.003	1.356	0.002	34.9	1.3	367	25
SLy	1.625	2.763	0.018	1.341	0.009	39.8	7.9	416	149
SLy	1.750	2.743	0.001	1.332	0.001	44.2	0.6	461	11
ALF2	1.000	2.963	0.002	1.489	0.001	38.9	0.6	415	11
ALF2	1.125	2.969	0.001	1.492	0.001	38.7	0.4	412	8
ALF2	1.250	2.950	0.004	1.482	0.002	41.3	1.6	439	31
ALF2	1.375	2.900	0.005	1.457	0.002	47.2	2.2	499	44
ALF2	1.500	2.881	0.002	1.448	0.001	50.3	1.2	530	22
ALF2	1.625	2.845	0.006	1.430	0.003	56.1	3.6	589	67
ALF2	1.750	2.799	0.004	1.407	0.002	63.5	3.3	664	60
H4	1.000	3.057	0.001	1.507	0.000	46.6	0.4	498	8
H4	1.125	3.037	0.003	1.497	0.001	49.6	1.4	528	26
H4	1.250	3.034	0.004	1.496	0.002	51.5	1.9	546	37
H4	1.375	3.029	0.001	1.494	0.001	54.3	0.6	574	11
H4	1.500	2.979	0.004	1.469	0.002	63.7	2.6	670	47
H4	1.625	2.911	0.002	1.435	0.001	77.4	1.7	810	32
H4	1.750	2.858	0.002	1.409	0.001	91.4	1.8	953	34

Bauswein formula. However, this formula cannot properly describe the behaviour shown by the data points belonging to the SLy EOS. The SLy data points clearly indicate a maximum for $q > 1$ (cmp. Fig. 7). An accounting for extrema of M_{thr} at $q > 1$ can be achieved by adding two linear terms to Eq. (16). The resulting fit formula with seven coefficients takes the form

$$M_{\text{thr}}(q, X, Y) = c_1 X + c_2 Y + c_3 + c_4 \delta\tilde{q} X + c_5 \delta\tilde{q} Y + c_6 \delta\tilde{q}^3 X + c_7 \delta\tilde{q}^3 Y. \quad (17)$$

The corresponding fits are visualized in Fig. 8, coefficients are reported in Tab. IX. The R^2 coefficients of these fits reach values of 0.97 and higher, with best results for the parameter pair $(X, Y) = (M_{\text{max}}, R_{\text{max}})$.

Considering again the fit formula by Bauswein et al. [16] (Eq. (16)), there are two general cases to distinguish: The case of monotonously (in q) decreasing M_{thr} and the case of monotonously (in q) increasing M_{thr} . Based on the findings of Bauswein et al., we will consider monotonously decreasing M_{thr} the typical case. However, as indicated by the gray colouring in Fig. 9 with respect to their findings there is room for speculation, as the fits given in [16] are based on data with $q \leq 1/0.7$. Considering our data, at the upper end of the studied mass-ratio interval, we find M_{thr} to decrease for all three EOSs. We therefore hypothesize this to be the general rule: The threshold mass as a function of the mass ratio

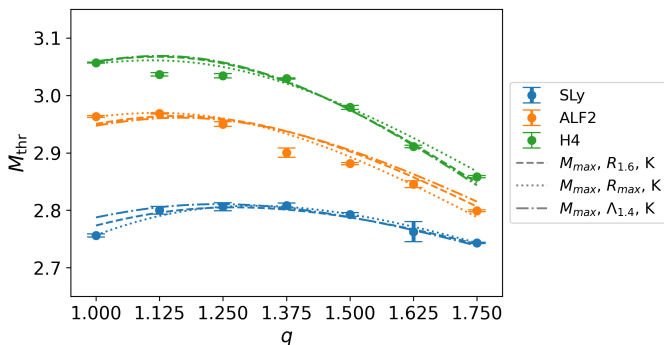


FIG. 8. Data points: same as in Fig. 7. Dashed/dotted lines: Fits to the data points depending on pairs of stellar parameters as given in the legend, based on Eq. (17) with coefficients given in Tab. IX.

can either decrease over the full mass ratio interval, or increase for small mass ratio, reaching a maximum before decreasing for high mass ratios. In a recently published study, Perego et al. [17] give a detailed discussion of the mass-ratio dependence of M_{thr} . Investigating the broad mass-ratio interval, $0.6 \leq \tilde{q} \leq 1.0$, and six EOS, they also find the threshold mass to decrease for $0.6 \leq \tilde{q} \leq 0.7$.

Another interesting feature worth mentioning is the small dip of M_{thr} presented in H4 for small deviations from $q = 1$. This is also reported by Bauswein et al. for the case of DD2F (cmp. Fig. 4 in [16]).

In Fig. 9 we directly compare our results for the threshold mass to results by Bauswein et al. [16] (crosses), and recently published results by Kashyap et al. [75] (stars). While Figs. 7 and 8 show fits of our data set (denominated K), Fig. 9 shows a sample of fits to data by Bauswein et al. [16], who distinguish between different subsets of their data, i.e., b, e, and h.

Overall, we find two thirds of our data in good agreement with the results of Bauswein et al. [16]. For the other third there are significant differences for $q = 1$ (SLy, H4) and for $q = 1/0.7$ (H4). Considering that the results are based on different numerical approaches, there is room for speculation about the exact source of these differences. We will instead infer from the comparability of individual results that results are comparable in the broader picture.

Kashyap et al. [75], who conducted simulations with the WhiskyTHC code (e.g., [82]), find systematic deviations of data by Bauswein et al. [16] from their results ($q = 1$). While for $q = 1$ threshold masses, found by Bauswein et al., are higher than any of respective data found by us or Kashyap et al., the same systematic can not be found for higher mass ratios, cf. Fig. 9, where data by Bauswein et al. tend to take on smaller values than our results for neighbouring mass ratios. A comparison of results by Kashyap et al. to our data shows small non-systematic differences.

Aside the direct comparison of data points, we compare our data points to fits by Bauswein et al., given

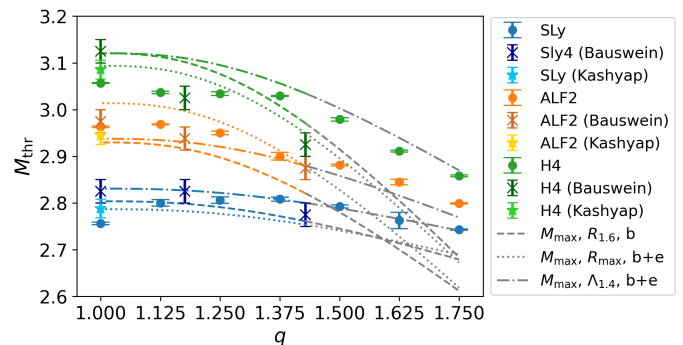


FIG. 9. Comparison of data and fits. Data points: As in Fig. 7. Crosses: Data by Bauswein et al. [16]. Stars: Data by Kashyap et al. [75]. Dashed/dotted lines: Fits as found by Bauswein et al. (cmp. Eq. (10), Fig. 5 and TABLE. VI of [16]) depending on pairs of stellar parameters. The underlying fits are based on different subsets (b, b+e) of data for $\tilde{q} = 1/q \in [0.7, 1.0]$ given in [16]. The transition to extrapolation beyond $q = 1/0.7$ is marked by a change to gray color.

in Tab. VI of Ref. [16]. These fits are characterized by different options for pairs of stellar parameters and data subsets. Plugging in the coefficients derived in [16], and stellar parameters characterizing our EOSs, we obtain the curves presented in Fig. 9. As marked in the legend of Fig. 9, the selected coefficients belong to data subsets denominated b and b+e.¹³

For each EOS the deviations between our results and their models typically increase for high mass ratios. These deviations at high mass ratios can be explained by the mass ratio range of the data underlying their fits. Though Bauswein et al. present one example of data in the wide range of $0.5 \leq \tilde{q} \leq 1.0$ in Fig. 4 of their work [16], the mass ratio range of the data underlying their fits is $0.7 \leq \tilde{q} \leq 1.0$. Therefore, the curves in Fig. 9 are extrapolations for $q > 1/0.7$ (indicated by the color change). However, one of the depicted cases, $(M_{\text{max}}, \Lambda_{1.4}, \text{b}+\text{e})$, agrees well with our data at high mass ratios.

Testing our fits (Fig. 8, Tab. IX) on the set (P) of data recently published by Perego et al. [17], we find that our fits do not properly predict their threshold-mass results. This observation holds true for all fits based on the parameter-pairs $(M_{\text{max}}, R_{1.6})$, $(M_{\text{max}}, R_{\text{max}})$, and $(M_{\text{max}}, \Lambda_{1.4})$. We expect this to be caused by the small amount of EOSs, which we covered during our study. However, by combining our data set (K) and the one of Ref. [17] (P), and giving up on the possibility to use only parameters extractable from the GW signals, we can improve the fitting. For this purpose, we employ the parameter pair $(X, Y) = (M_{\text{max}}, \hat{M}_{\text{thr}}(q = 1))$, where $\hat{M}_{\text{thr}}(q = 1)$ is the estimated threshold mass at $q = 1$

¹³ The letter b denotes their *base sample of hadronic EOSs*, the subset b+e also contains *excluded hadronic EOSs*, to which they also count H4.

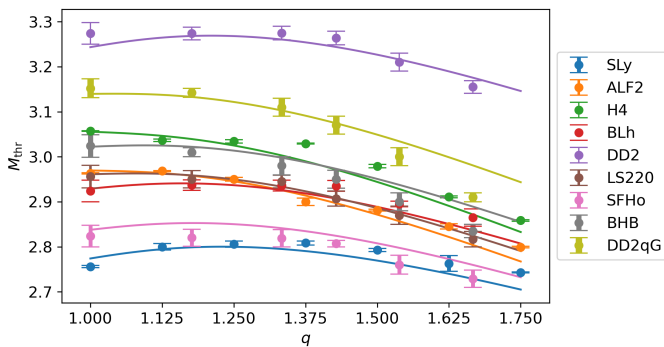


FIG. 10. Fit of the data set K+P, which includes data by Perego et al. [17]. The fit is based on Eq. (17) and the parameter pair $(X, Y) = (M_{\max}, M_{\text{thr}}(q = 1))$. Coefficients are given in Tab. X.

based on the simulation data; fitting coefficients are provided in Tab. X. As shown in Fig. 10 this procedure allows to capture reliably the mass-ratio dependence of the threshold mass for a large set of EOSs.

E. Mass Ratio Effects on κ_2^{T} and $\tilde{\Lambda}$

As stated in [11], based on the analysis of data from the CoRe collaboration for the case of prompt-collapse mergers, the tidal polarizability parameter κ_2^{T} and coefficient $\tilde{\Lambda}$ take on values captured by the inequalities:

$$\kappa_2^{\text{T}} < (\kappa_2^{\text{T}})_{\text{thr}} \sim 80 \pm 40, \quad (18)$$

$$\tilde{\Lambda} < \tilde{\Lambda}_{\text{thr}} \sim 362 \pm 24, \quad (19)$$

with $(\kappa_2^{\text{T}})_{\text{thr}}$ and $\tilde{\Lambda}_{\text{thr}}$ marking the upper limit in the prompt-collapse case. In this chapter, we compare these inequalities to our own findings, and provide mass ratio and EOS dependent relations in place of the constants on the right-hand side.

To provide insight into the tidal deformabilities accessed by our simulations, we present κ_2^{T} and $\tilde{\Lambda}$ against the total mass M in Fig. 11 (upper row) for all mass ratios and EOSs. We distinguish between prompt-collapse (coloured points) and delayed-collapse (gray points) and mark quantities at $M = M_{\text{thr}}$ with crosses.¹⁴

In the second row of Fig. 11 the quantities at threshold are given as functions of the mass ratio q .

Considering the presented data we point out two observations:

- Relation (18) is met by all data points presented in Fig. 11 (cmp. panel on the upper left).

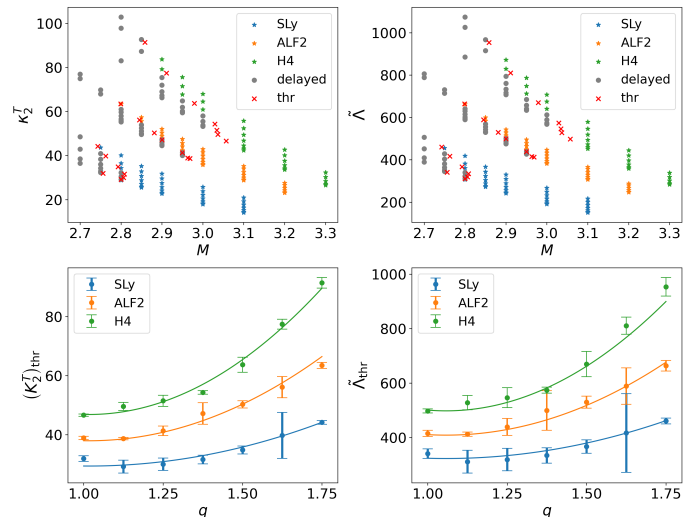


FIG. 11. Upper row: Tidal polarizability parameter κ_2^{T} (first column) and tidal polarizability coefficient $\tilde{\Lambda}$ (second column) plotted against the total mass M . Included are all collapse scenarios. Colours distinguish prompt-collapse scenarios (blue, orange, green) from delayed-collapse scenarios (gray). Crosses mark quantities at the threshold to prompt collapse as calculated from M_{thr} . Lower row: tidal polarizability quantities at the threshold to prompt collapse as a function of the mass ratio q . Solid lines are fits over all data using Eq. (20).

- Relation (19) captures only a small number of our threshold data points (cmp. panel on the lower right of Fig. 11).

To improve these inequalities, we present mass ratio and EOS dependent fits to model the tidal deformability of BNSs at threshold to prompt collapse. The fits illustrated in the lower panels of Fig. 11 are least squares fits to all 21 threshold data-points. The fit formula applied to $Z_{\text{tidal}} \in \{\kappa_2^{\text{T}}, \tilde{\Lambda}\}$ is a polynomial of second order in q ,

$$Z_{\text{tidal}}^{\text{thr}} = c_1 + c_2 \tilde{\Lambda}_{1.4} + c_3 \tilde{\Lambda}_{1.4} q + c_4 \tilde{\Lambda}_{1.4} q^2, \quad (20)$$

that adequately models the dependence of $Z_{\text{tidal}}^{\text{thr}}$ on the studied EOSs. The coefficients c_1 to c_4 are given in Tab. V. As κ_2^{T} and $\tilde{\Lambda}$ are decreasing in M , the following relation holds for a BNS of given mass ratio and EOS in connection with the tidal quantity Z_{thr} at threshold

$$Z_{\text{tidal}}^{\text{delayed}} > Z_{\text{tidal}}^{\text{thr}}(q) > Z_{\text{tidal}}^{\text{prompt}}. \quad (21)$$

F. Disk Mass and Remnant BH Properties - Qualitative Discussion

In this section, we qualitatively discuss the effect of the mass ratio on the disk mass, the BH mass M_{BH} , and the BH spin χ_{BH} , distinguishing between delayed and prompt-collapse BNS-mergers. In the following section we build upon this discussion, proposing, for the case

¹⁴ The distinction between prompt and delayed collapse, highlighted by the color changes in Fig. 11, is based on the respective collapse times, not on M compared to M_{thr} .

TABLE V. Fits describing the EOS dependence of the tidal polarizability parameter κ_2^T and the tidal polarizability coefficient $\tilde{\Lambda}$ of BNS configurations at the threshold to prompt collapse as a function of the mass ratio q . We also present the following measures of variation: the maximal relative residual (max.), the mean absolute residual (av.), and the coefficient of determination (R^2).

$$Z_{\text{tidal}}^{\text{thr}} = c_1 + c_2 \tilde{\Lambda}_{1.4} + c_3 \tilde{\Lambda}_{1.4} q + c_4 \tilde{\Lambda}_{1.4} q^2$$

$Z_{\text{tidal}}^{\text{thr}}$	$(\kappa_2^T)_{\text{thr}}$	$\tilde{\Lambda}_{\text{thr}}$
c_1	19.9 ± 1.2	221 ± 21
c_2	0.123 ± 0.019	1.40 ± 0.342
c_3	-0.183 ± 0.029	-2.07 ± 0.54
c_4	0.090 ± 0.011	0.98 ± 0.20
max.	7.0%	6.9%
av.	1.173	14.86
R^2	0.9907	0.9839

of prompt-collapse mergers, approximate models of the matter maximally accumulated in the disk and the minimal BH mass.

1. Ejection Mechanisms and Disk Mass

The amount of material ejected or accumulated in the disk surrounding the BH depends on multiple factors, e.g., the total mass of the system, the mass ratio, and the EOS. Further, the categories *prompt* and *delayed collapse* are a useful distinction of cases, though the type of the merger is not independent of M , q , and the EOS. Previous studies have identified different mechanisms responsible for the ejection of matter. In Ref. [79] Hotokezaka et al. studied the mass ejection from BNS mergers for small mass ratios, $1 \leq q \leq 1/0.8$, distinguishing the cases of HMNS and BH remnants. In the case of HMNS remnants they find larger amounts of ejected material compared to the case of BH remnants. Comparing unequal-mass binaries to equal-mass binaries, on the other hand, the amount of ejected material is larger in the asymmetric case. They considered two ejection mechanisms: One mechanism is shock heating which plays no important role in the BH remnant case, but works efficiently to eject material from HMNSs. The second mechanism is ejection due to angular momentum transport/torque exerted during merger. In the case of unequal-mass binaries, where the less massive component gets tidally elongated during merger, they find this to be the ejection mechanism dominating the first few milliseconds after the onset of merger. Parts of the tidal tails, formed due to tidal elongation of the less massive component, will remain in a rotationally supported disk [82]. In the case of HMNS remnants, further material can be ejected due to ongoing shocks for tenths of milliseconds.

Another ejection mechanism has been investigated by Bernuzzi et al. in [83], who study accretion induced prompt BH formation of ten binary configurations. Com-

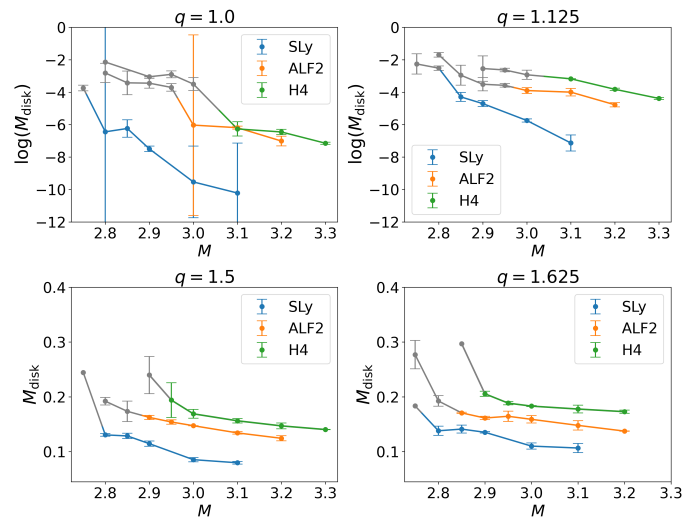


FIG. 12. Disk mass M_{disk} 5 ms after t_{AH} as a function of the total mass M for a sample of four mass ratios. Connected data points belong to the same EOS. Delayed-collapse mergers are marked in gray. In the case of prompt collapse, for a given EOS and mass ratio, the disk mass is smaller compared to the case of delayed collapse.

paring equal-mass cases to high mass ratio cases, they find that for highly asymmetric binaries the more massive component tidally disrupts its companion, therefore producing large amounts of ejected material.

A broad mass-ratio-range study up to about $q \sim 2$, has been conducted by Dietrich et al. [74]. They found that in prompt-collapse scenarios, in contrast to delayed-collapse scenarios, no massive disk is formed. As discussed by Bernuzzi et al. in [83], the bulk of dynamical ejecta from BNS mergers is connected to the bounce of NS cores, cf. also [82]. As the absence of a core-bounce is equivalent to the prompt-collapse criterion of monotonically decreasing maximum-density, this ejection mechanism is expected to be suppressed in prompt-collapse scenarios, and only small amounts of material are expected to be ejected, or to be accumulated in the disk, due to this effect.

In a nutshell, compared to the case of equal-mass BNS mergers, the amount of material ejected or gathered in a disk around the remnant, is larger for unequal-mass binaries. EOS and mass ratio are more dominant factors than the total mass of the binary. More material is ejected the longer the remnant HMNS evades collapse.

Many of the findings summarized above are mirrored in our finding for the disk mass. In Fig. 12, for a sample of two small and two high mass ratios, the disk mass is plotted against the total mass M . There is a vast difference between the disk mass in case of small mass ratios compared to the case of highly asymmetric binaries. This is already visible in the scaling of the axes. For $q = 1.0$ and $q = 1.125$ the highest disk masses found in our simulations are at the order of $\sim 0.01 M_{\odot}$. In the prompt-collapse case of equal-mass binaries it is less than $10^{-4} M_{\odot}$. This highlights the dominant role that

the mass ratio plays in the context of ejecta from BNS mergers.

2. BH remnant

The effects of mass ratio on the remnant BH are best discussed from the perspective gained in the previous discussion. Following this line of thought, we will forgo the discussion of other effects than those connected to the ejection of matter/ formation of a disk. To support the following argumentation, we define the mass ratios, Q_{disk} and Q_{BH} :

$$Q_{\text{disk}} := \frac{M_{\text{disk}}}{M^{\text{b}}}, \quad (22)$$

$$Q_{\text{BH}} := \frac{M_{\text{BH}}}{M}, \quad (23)$$

relating the disk mass to the initial baryonic mass M^{b} , and the BH mass to the total mass of the binary. In the case of prompt collapse, we find to find M_{BH} to grow almost linearly with the total mass M . Considering the newly defined ratio Q_{BH} this corresponds to the almost constant slope which we find for high M in Fig. 16. On the other hand we find a strong decrease of Q_{BH} in the case of delayed collapse, i.e., for small total masses and more prominently in the case of unequal-mass binaries, cf. Fig. 16. Comparing Figs. 12 and 16, this decrease of M_{BH} relates well to the increased disk mass in these cases. Considering Figs. 14 to 15 we find both M_{BH} and χ_{BH} to decrease for high mass ratios, while the fraction Q_{disk} increases (cmp. Fig. 13), i.e., both the BH's mass and its spin decrease with increasing amounts of material being either ejected or accumulated in the disk. Both M_{BH} and χ_{BH} are increasing with M .

G. Disk Mass and Remnant BH Properties - Estimating Quantities at Threshold

Distinguishing the cases of prompt and delayed collapse, the inequalities

$$Z_{\text{disk}}^{\text{delayed}} \geq Z_{\text{disk}}^{\text{thr}}(q) \geq Z_{\text{disk}}^{\text{prompt}}, \quad (24)$$

$$Z_{\text{BH}}^{\text{delayed}} \leq Z_{\text{BH}}^{\text{thr}}(q) \leq Z_{\text{BH}}^{\text{prompt}}, \quad (25)$$

hold for the quantities considered in connection with disk and BH mass, i.e., $Z_{\text{disk}} \in \{M_{\text{disk}}, Q_{\text{disk}}\}$ and $Z_{\text{BH}} \in \{M_{\text{BH}}, Q_{\text{BH}}\}$, cf. Figs. 12 and 16, and discussion in the previous section. For each case, (q , EOS), upper (lower) estimates of Z_{disk} and Z_{BH} in prompt-collapse cases can be obtained by approximating the quantities at threshold with the maximal (minimal) value of the respective prompt-collapse regime (cf. data points in Fig. 17).¹⁵

¹⁵ In the case of the disk, the threshold quantities $Z_{\text{disk}}^{\text{thr}}$ are approximated by the highest values found for prompt-collapse configura-

TABLE VI. Fits describing the estimates for the behaviour of the remnant BH mass close to the threshold to prompt collapse. For each EOS and mass ratio, the BH mass at threshold is approximated by the minimal BH-mass value for the case of prompt-collapse mergers. The fit formula given below depends on a pair of stellar parameters: $(X, Y) = (M_{\text{max}}, \Lambda_{1.4})$. We present the following measures of variation: the maximal relative residual (max.), the mean absolute residual (av.), and the coefficient of determination (R^2).

Fit formula given in $\begin{cases} \text{Eq. (27), } Z_{\text{BH}} = M_{\text{BH}} \\ \text{Eq. (28), } Z_{\text{BH}} = Q_{\text{BH}} \end{cases}$		
$Z_{\text{BH}}^{\text{thr}}$	$M_{\text{BH}}^{\text{thr}}$	$Q_{\text{BH}}^{\text{thr}}$
c_1	0.45 ± 0.01	0.431 ± 0.003
c_2	$(9.101 \pm 0.989) \cdot 10^{-4}$	$(6.388 \pm 0.284) \cdot 10^{-4}$
c_3	0.104 ± 0.016	0.021 ± 0.002
c_4	0.943 ± 0.312	-0.564 ± 0.173
c_5	2.294 ± 0.768	2.428 ± 0.545
c_6	$(9.644 \pm 0.777) \cdot 10^{-4}$	$(3.837 \pm 0.108) \cdot 10^{-4}$
max.	0.0618	0.765
av.	0.0234	0.239
R^2	0.952	0.971

To model the effect of mass ratio on disk and BH properties, we fit the approximated threshold quantities Z_{disk} and Z_{BH} by means of a least squares approach, using the fit formulae

$$Z_{\text{disk}}^{\text{thr}} = A \cdot \{1.0 + \tanh [M_{\text{max}} (c_3 + c_4 q)] + c_5 M_{\text{max}}\}, \quad (26)$$

$$M_{\text{BH}}^{\text{thr}} = A \cdot \{2.5 - c_3 \tanh [M_{\text{max}} (c_4 + c_5 q)] - c_6 \Lambda_{1.4}\}, \quad (27)$$

$$Q_{\text{BH}}^{\text{thr}} = A \cdot \{1.0 + c_3 \tanh [M_{\text{max}} (c_4 + c_5 q)] - c_6 \Lambda_{1.4}\}. \quad (28)$$

$$A = (c_1 M_{\text{max}} + c_2 \Lambda_{1.4}),$$

The respective fits are presented in Fig. 17, and coefficients are reported in Tabs. VI and VII. Because of the approximating character of this threshold model, the inequalities (24) and (25) take the form

$$Z_{\text{disk}}^{\text{delayed}} \gtrsim Z_{\text{disk}}^{\text{thr}} \gtrsim Z_{\text{disk}}^{\text{prompt}}, \quad (29)$$

$$Z_{\text{BH}}^{\text{delayed}} \lesssim Z_{\text{BH}}^{\text{thr}} \lesssim Z_{\text{BH}}^{\text{prompt}}. \quad (30)$$

As discussed in Sec. IV F, ejection mechanism except for tidal effects are suppressed in the case of prompt-collapse mergers. Therefore the data/fits presented in first column of Fig. 17 visualize, how the strength of tidal effects

tions. An alternative approach would be to interpolate between the data points below and above threshold. Considering the lack of data in some cases, where none of the simulated configurations produced a delayed collapse, we will go with the described method, which might lead to a systematic overestimation of the quantities at threshold by up to a few percent. A similar statement holds for other quantities considered in this section.

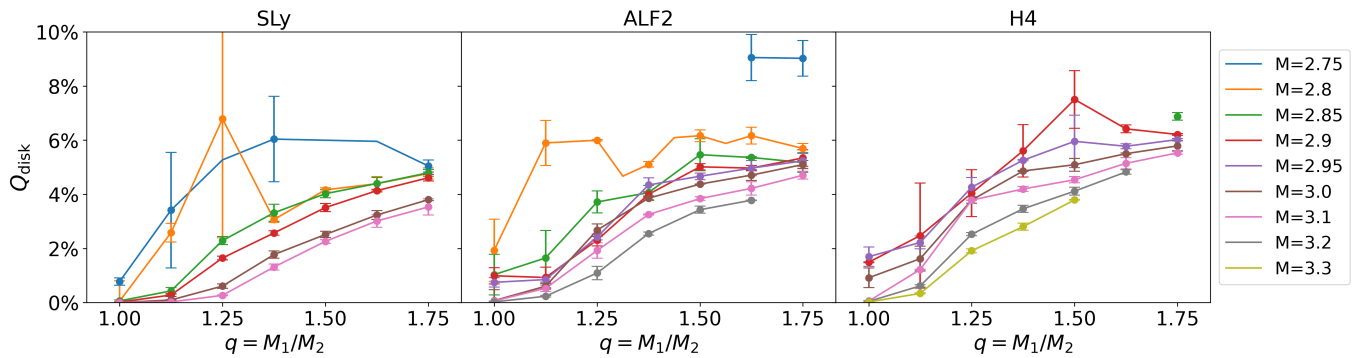


FIG. 13. Disk mass as a fraction of the initial total baryonic mass M^b of the BNS 5 ms after t_{AH} as a function of q . Connected data points correspond to fixed values of the total mass M and belong to simulations where a BH was formed within simulation time. Data are grouped with respect to EOS and presented in separate panels. The fraction of mass accumulated in the disk is typically higher for lower values of M and for high mass ratios.

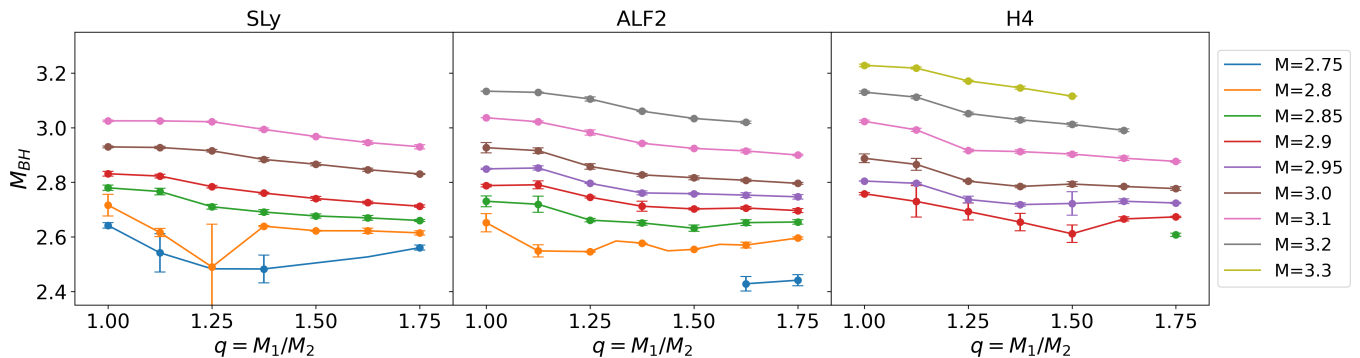


FIG. 14. Mass M_{BH} of the BH remnant 5 ms after t_{AH} as a function of q . Connected data points correspond to fixed values of M . Data are grouped with respect to EOS and presented in separate panels. The BH remnant's mass is higher the higher the initial BNS's total mass M . For high total masses M , M_{BH} decreases monotonously for increasing mass ratio.

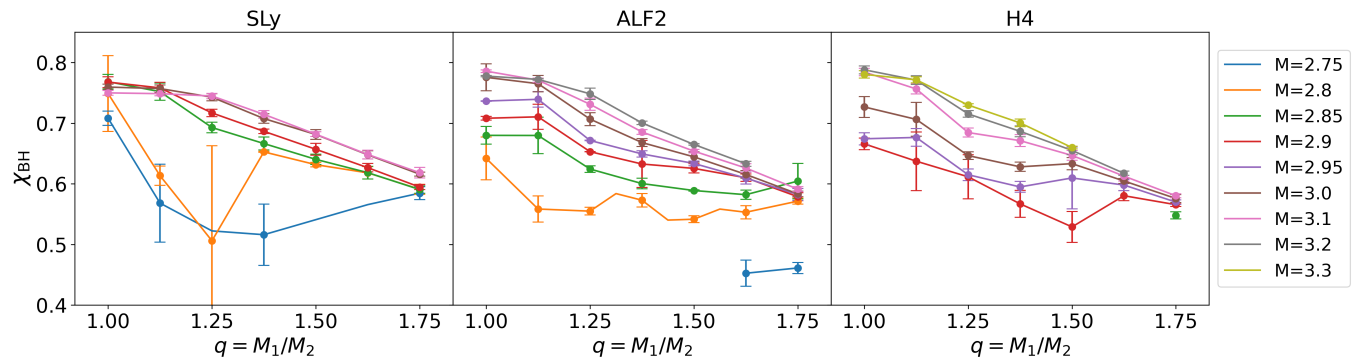


FIG. 15. Spin χ_{BH} of the BH remnant 5 ms after t_{AH} as a function of q . Connected data points correspond to fixed values of M . Data are grouped with respect to EOS and presented in separate panels. For fixed mass ratio the BH spin increases with the total mass M . For the highest values of M in each panel, the BH spin is a monotonously decreasing function in the mass ratio q , for lower values of M the functional relation between χ and q becomes less clear.

(tidal elongation, tidal disruption) at the onset of merger is effected by the mass ratio. While for symmetric binaries the disk mass is negligible, the disk mass increases for increasing mass ratios. A similar effect is to be expected for the amount of matter ejected from the system.

V. COLLAPSE TIME AT THRESHOLD

Additional to the set of simulations presented in Tabs. XI to XVI (appendix), we have performed simulations of BNS configurations with total masses close to the threshold mass determined for the case of $q = 1.5$ with ALF2. These additional simulations revealed a substruc-

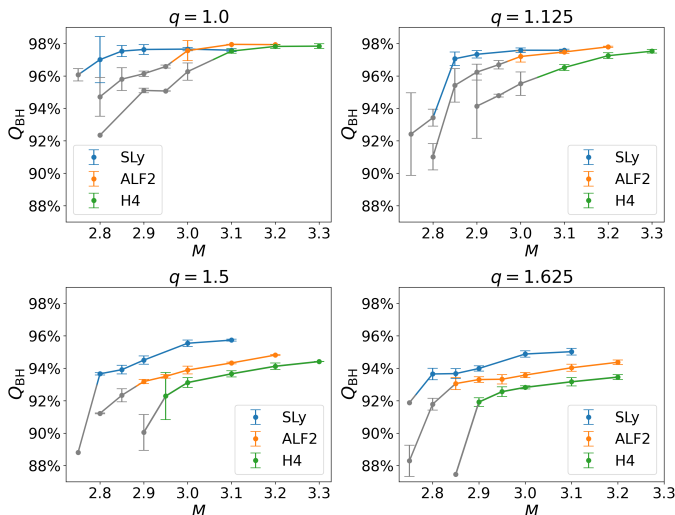


FIG. 16. Mass of the BH remnant as a fraction of the total mass M 5 ms after t_{AH} presented as a function of the total mass M ; sample of four mass ratios. Connected data points belong to the same EOS and delayed-collapse mergers are marked in gray. For given EOS and mass ratio, the Q_{BH} increases with M .

TABLE VII. Fits describing the estimates for the behaviour of the disk mass close to the threshold to prompt collapse. For each EOS and mass ratio, the disk mass at threshold is approximated by the maximal disk-mass value for the case of prompt-collapse mergers. The fit formula given below depends on a pair of stellar parameters: $(X, Y) = (M_{\text{max}}, \Lambda_{1.4})$. We present the following measures of variation: the maximal relative residual (max.), the mean absolute residual (av.), and the coefficient of determination (R^2).

Fit formula given in Eq. (26)		
$Z_{\text{disk}}^{\text{thr}}$	$M_{\text{disk}}^{\text{thr}}$	$Q_{\text{disk}}^{\text{thr}}$
c_1	0.031 ± 0.004	0.011 ± 0.001
c_2	$(6.274 \pm 0.95) 10^{-5}$	$(1.836 \pm 0.311) 10^{-5}$
c_3	-0.506 ± 0.13	-0.474 ± 0.13
c_4	2.278 ± 0.4	2.048 ± 0.377
c_5	-0.119 ± 0.071	-0.132 ± 0.075
max.	0.0242	0.00709
av.	0.00657	0.00215
R^2	0.983	0.982

ture within the collapse-time curve which has not been resolved for mass steps $\Delta M \geq 0.05$. We present these data points in the second and third panel of Fig. 18 together with the seven data points used for the localization of M_{thr} , which are depicted in the first panel. The additional data indicate that the collapse-time curve changes abruptly its slope in the vicinity of the threshold mass. To understand the behaviour of the collapse time at threshold further studies with different EOSs and mass ratios are needed.

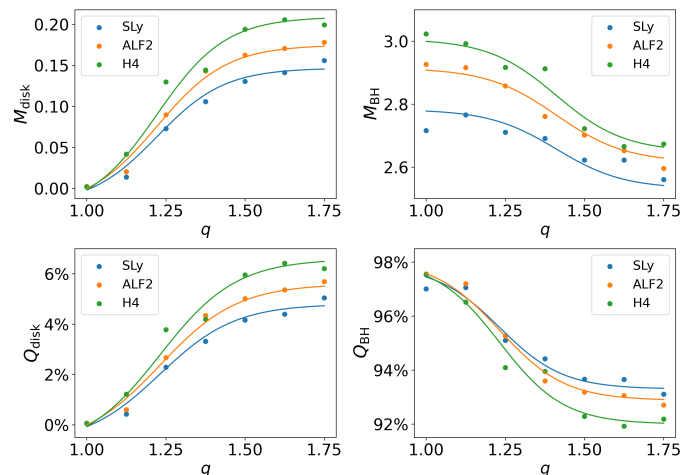


FIG. 17. First column: Fits of the disk-mass estimates, M_{disk} , and mass ratio Q_{disk} , close to threshold. The fit formula given in Eq. (26) depends on the pair of stellar parameters: $(X, Y) = (M_{\text{max}}, \Lambda_{1.4})$. Data points: maximum value of M_{disk} (upper panel) and Q_{disk} (lower panel) for given EOS and mass ratio for the case of prompt collapse.

Second column: Fits of the BH-mass estimates, M_{BH} , and mass ratio, Q_{BH} , close to threshold. The fit formulae given in Eqs. (27) and (28) depend on a pair of stellar parameters: $(X, Y) = (M_{\text{max}}, \Lambda_{1.4})$. Data points: minimum values of M_{BH} (upper panel) and Q_{BH} (lower panel) for given EOS and mass ratio for the case of prompt collapse.

VI. SUMMARY AND OUTLOOK

This paper reviews definitions and criteria in connection with the threshold mass to prompt collapse in BNS mergers, as well as methods to determine the collapse time within NR simulations. We show that the way to measure collapse time used in this work and a method based on the minimum-lapse function, recently updated in [18] compared to [14], are consistent within deviations at the order of tenth of milliseconds. Based on results from a large set of 290 fully general relativistic simulations covering three equations of state, and seven mass ratios with different total masses, we propose a new method for localizing the threshold mass.

This method is based on a fitting procedure and the definition of a threshold collapse time, τ_{thr} , which presumably can be assigned to the threshold mass independently of the EOS. The definition of τ_{thr} is empirically motivated, and happens within a certain tolerance, due to the shape of the collapse-time curve in the vicinity of M_{thr} . The fit function is constructed such that the typically used bracketing method can be included easily by setting bounds to one of the fit parameters. This fit is used to determine M_{thr} as the value of M that satisfies $t_{\text{coll}}(M) = \tau_{\text{thr}}$.

To study the effect of mass ratio, we apply this method to our data, determining the threshold mass for seven mass ratios in the range $1.0 \leq q \leq 1.75$ per EOS. To

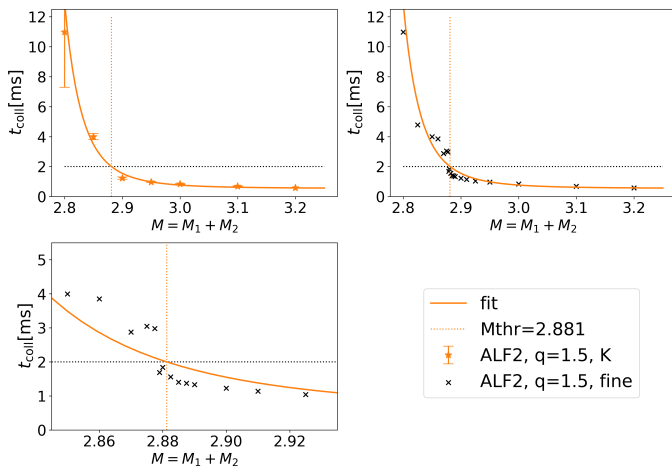


FIG. 18. Collapse time in the case of $q = 1.5$ with ALF2. First panel: Seven data points and fit as presented in Fig. 6. The vertical dotted line marks the threshold mass as determined by the method introduced in Sec. IV C. Second panel: Displayed are the same data and fit as in the first panel together with results from additional R3 simulations for total masses close to the marked threshold mass. Third panel: Close-up of the second panel.

obtain error estimates on individual data points, we perform evolutions with different numerical resolutions. We analyse these results making comparisons with results obtained by Bauswein *et al.* [16], who have conducted a survey of 40 EOS finding fits for the threshold mass as a function of the mass ratio based on three data points per EOS for mass ratios $0.7 \leq 1/q \leq 1.0$. Discussing consistencies and deviations, we present fits to our data using their original fit formula as well as an extended version that accounts for additional behaviours in the threshold mass data sets (maxima at $q > 1$). Considering the threshold mass as a function of q , we find the same

qualitative behaviour at the upper end of the mass-ratio interval, independent of the EOS. For small and medium mass ratios on the other hand, with regard to the EOS, different scenarios are possible.

Investigating the effect of the mass ratio on the tidal polarizability of BNSs at threshold, characterized by the quantities κ_2^T and $\tilde{\Lambda}$, we improve on relations describing the tidal deformability of prompt-collapse mergers, given in [11] and [15], by modelling the mass-ratio and EOS dependence of the tidal deformability at threshold. Moreover, we present approximate models for the mass-ratio dependence of BH and disk mass at threshold.

Finally, for total masses close to the threshold mass M_{thr} , we find an interesting substructure in the shape of the collapse-time curve. This phenomenon needs further study with regard to EOSs and mass ratios.

In our work we consider irrotational BNSs, the effect of NS spin will be the topic of a follow-up study. Also, our simulations do not treat the effects of neutrino transport and magnetic fields. Compared to the impact of EOSs, we presume these effects to play a minor role, especially in the case of prompt-collapse mergers.

ACKNOWLEDGMENTS

We thank Wolfgang Tichy for his support with the SGRID code. M.K. acknowledges support from the Deutsche Forschungsgemeinschaft (DFG) under Grant No. 406116891 within the Research Training Group RTG 2522/1. M.U. acknowledges support through the Coordenação de Aperfeiçoamento de Pessoal de Nível Superior - Brasil (CAPES) - Process number: 88887.571346/2020-00. T.D. acknowledges financial support through the Max Planck Society.

Computations were performed on HAWK at the High-Performance Computing Center Stuttgart (HLRS) [project GWanalysis 44189] and on the ARA cluster of the University of Jena.

-
- [1] B. P. Abbott *et al.* (Virgo, LIGO Scientific), GW170817: Observation of Gravitational Waves from a Binary Neutron Star Inspiral, *Phys. Rev. Lett.* **119**, 161101 (2017), [arXiv:1710.05832 \[gr-qc\]](#).
 - [2] B. P. Abbott *et al.* (Virgo, Fermi-GBM, INTEGRAL, LIGO Scientific), Gravitational Waves and Gamma-Rays from a Binary Neutron Star Merger: GW170817 and GRB 170817A, *Astrophys. J.* **848**, L13 (2017), [arXiv:1710.05834 \[astro-ph.HE\]](#).
 - [3] B. Abbott *et al.* (LIGO Scientific, Virgo), GW190425: Observation of a Compact Binary Coalescence with Total Mass $\sim 3.4M_{\odot}$, *Astrophys. J. Lett.* **892**, L3 (2020), [arXiv:2001.01761 \[astro-ph.HE\]](#).
 - [4] M. W. Coughlin, T. Dietrich, S. Antier, M. Bulla, F. Foucart, K. Hotokezaka, G. Raaijmakers, T. Hinderer, and S. Nissanke, Implications of the search for optical counterparts during the first six months of the Advanced LIGO's and Advanced Virgo's third observing run: possible limits on the ejecta mass and binary properties, *Mon. Not. Roy. Astron. Soc.* **492**, 863 (2020), [arXiv:1910.11246 \[astro-ph.HE\]](#).
 - [5] R. Dudi, A. Adhikari, B. Brügmann, T. Dietrich, K. Hayashi, K. Kawaguchi, K. Kiuchi, K. Kyutoku, M. Shibata, and W. Tichy, Investigating GW190425 with numerical-relativity simulations (2021), [arXiv:2109.04063 \[astro-ph.HE\]](#).
 - [6] B. P. Abbott *et al.* (LIGO Scientific, Virgo), Properties of the binary neutron star merger GW170817, *Phys. Rev. X* **9**, 011001 (2019), [arXiv:1805.11579 \[gr-qc\]](#).
 - [7] L.-X. Li and B. Paczynski, Transient events from neutron star mergers, *Astrophys. J.* **507**, L59 (1998), [arXiv:astro-ph/9807272 \[astro-ph\]](#).
 - [8] B. Metzger, G. Martinez-Pinedo, S. Darbha, E. Quataert, A. Arcones, *et al.*, Electromagnetic Counterparts of Com-

- compact Object Mergers Powered by the Radioactive Decay of R-process Nuclei, *Mon.Not.Roy.Astron.Soc.* **406**, 2650 (2010), [arXiv:1001.5029 \[astro-ph.HE\]](#).
- [9] L. F. Roberts, D. Kasen, W. H. Lee, and E. Ramirez-Ruiz, Electromagnetic Transients Powered by Nuclear Decay in the Tidal Tails of Coalescing Compact Binaries, *Astrophys.J.* **736**, L21 (2011), [arXiv:1104.5504 \[astro-ph.HE\]](#).
- [10] D. Kasen, B. Metzger, J. Barnes, E. Quataert, and E. Ramirez-Ruiz, Origin of the heavy elements in binary neutron-star mergers from a gravitational wave event, *Nature*, 10.1038/nature24453 10.1038/nature24453 (2017), [arXiv:1710.05463 \[astro-ph.HE\]](#).
- [11] S. Bernuzzi, Neutron Star Merger Remnants, *Gen. Rel. Grav.* **52**, 108 (2020), [arXiv:2004.06419 \[astro-ph.HE\]](#).
- [12] K. Hotokezaka, K. Kyutoku, H. Okawa, M. Shibata, and K. Kiuchi, Binary Neutron Star Mergers: Dependence on the Nuclear Equation of State, *Phys.Rev.* **D83**, 124008 (2011), [arXiv:1105.4370 \[astro-ph.HE\]](#).
- [13] A. Bauswein, T. Baumgarte, and H. T. Janka, Prompt merger collapse and the maximum mass of neutron stars, *Phys.Rev.Lett.* **111**, 131101 (2013), [arXiv:1307.5191 \[astro-ph.SR\]](#).
- [14] S. Köppel, L. Bovard, and L. Rezzolla, A General-relativistic Determination of the Threshold Mass to Prompt Collapse in Binary Neutron Star Mergers, *Astrophys. J. Lett.* **872**, L16 (2019), [arXiv:1901.09977 \[gr-qc\]](#).
- [15] M. Agathos, F. Zappa, S. Bernuzzi, A. Perego, M. Breschi, and D. Radice, Inferring Prompt Black-Hole Formation in Neutron Star Mergers from Gravitational-Wave Data, *Phys. Rev. D* **101**, 044006 (2020), [arXiv:1908.05442 \[gr-qc\]](#).
- [16] A. Bauswein, S. Blacker, G. Lioutas, T. Soutanis, V. Vijayan, and N. Stergioulas, Systematics of prompt black-hole formation in neutron star mergers, *Phys. Rev. D* **103**, 123004 (2021), [arXiv:2010.04461 \[astro-ph.HE\]](#).
- [17] A. Perego, D. Logoteta, D. Radice, S. Bernuzzi, R. Kashyap, A. Das, S. Padamata, and A. Prakash, Probing the incompressibility of nuclear matter at ultrahigh density through the prompt collapse of asymmetric neutron star binaries (2021), [arXiv:2112.05864 \[astro-ph.HE\]](#).
- [18] S. D. Tootle, L. J. Papenfort, E. R. Most, and L. Rezzolla, Quasi-universal behaviour of the threshold mass in unequal-mass, spinning binary neutron-star mergers (2021), [arXiv:2109.00940 \[gr-qc\]](#).
- [19] W. Tichy, A. Rashti, T. Dietrich, R. Dudi, and B. Brügmann, Constructing binary neutron star initial data with high spins, high compactnesses, and high mass ratios, *Phys. Rev. D* **100**, 124046 (2019), [arXiv:1910.09690 \[gr-qc\]](#).
- [20] T. Dietrich, N. Moldenhauer, N. K. Johnson-McDaniel, S. Bernuzzi, C. M. Markakis, B. Brügmann, and W. Tichy, Binary Neutron Stars with Generic Spin, Eccentricity, Mass ratio, and Compactness - Quasi-equilibrium Sequences and First Evolutions, *Phys. Rev.* **D92**, 124007 (2015), [arXiv:1507.07100 \[gr-qc\]](#).
- [21] W. Tichy, Long term black hole evolution with the BSSN system by pseudo-spectral methods, *Phys.Rev.* **D80**, 104034 (2009), [arXiv:0911.0973 \[gr-qc\]](#).
- [22] W. Tichy, A New numerical method to construct binary neutron star initial data, *Class.Quant.Grav.* **26**, 175018 (2009), [arXiv:0908.0620 \[gr-qc\]](#).
- [23] W. Tichy, Black hole evolution with the BSSN system by pseudo-spectral methods, *Phys.Rev.* **D74**, 084005 (2006), [arXiv:gr-qc/0609087 \[gr-qc\]](#).
- [24] J. Wilson and G. Mathews, Instabilities in Close Neutron Star Binaries, *Phys.Rev.Lett.* **75**, 4161 (1995).
- [25] J. Wilson, G. Mathews, and P. Marronetti, Relativistic numerical model for close neutron star binaries, *Phys.Rev.* **D54**, 1317 (1996), [arXiv:gr-qc/9601017 \[gr-qc\]](#).
- [26] J. York, James W., Conformal 'thin sandwich' data for the initial-value problem, *Phys.Rev.Lett.* **82**, 1350 (1999), [arXiv:gr-qc/9810051 \[gr-qc\]](#).
- [27] M. J. Berger and J. Olinger, Adaptive Mesh Refinement for Hyperbolic Partial Differential Equations, *J.Comput.Phys.* **53**, 484 (1984).
- [28] S. Bernuzzi and T. Dietrich, Gravitational waveforms from binary neutron star mergers with high-order weighted-essentially-nonoscillatory schemes in numerical relativity, *Phys. Rev.* **D94**, 064062 (2016), [arXiv:1604.07999 \[gr-qc\]](#).
- [29] T. Dietrich, S. Bernuzzi, M. Ujevic, and B. Brügmann, Numerical relativity simulations of neutron star merger remnants using conservative mesh refinement, *Phys. Rev.* **D91**, 124041 (2015), [arXiv:1504.01266 \[gr-qc\]](#).
- [30] M. Thierfelder, S. Bernuzzi, and B. Brügmann, Numerical relativity simulations of binary neutron stars, *Phys.Rev.* **D84**, 044012 (2011), [arXiv:1104.4751 \[gr-qc\]](#).
- [31] B. Brügmann, J. A. Gonzalez, M. Hannam, S. Husa, U. Sperhake, *et al.*, Calibration of Moving Puncture Simulations, *Phys.Rev.* **D77**, 024027 (2008), [arXiv:gr-qc/0610128 \[gr-qc\]](#).
- [32] S. Bernuzzi and D. Hilditch, Constraint violation in free evolution schemes: comparing BSSNOK with a conformal decomposition of Z4, *Phys. Rev.* **D81**, 084003 (2010), [arXiv:0912.2920 \[gr-qc\]](#).
- [33] D. Hilditch, S. Bernuzzi, M. Thierfelder, Z. Cao, W. Tichy, *et al.*, Compact binary evolutions with the Z4c formulation, *Phys. Rev.* **D88**, 084057 (2013), [arXiv:1212.2901 \[gr-qc\]](#).
- [34] C. Bona, J. Massó, J. Stela, and E. Seidel, A class of hyperbolic gauge conditions, in *The Seventh Marcel Grossmann Meeting: On Recent Developments in Theoretical and Experimental General Relativity, Gravitation, and Relativistic Field Theories*, edited by R. T. Jantzen, G. M. Keiser, and R. Ruffini (World Scientific, Singapore, 1996).
- [35] M. Alcubierre, B. Brügmann, P. Diener, M. Koppitz, D. Pollney, *et al.*, Gauge conditions for long term numerical black hole evolutions without excision, *Phys.Rev.* **D67**, 084023 (2003), [arXiv:gr-qc/0206072 \[gr-qc\]](#).
- [36] J. R. van Meter, J. G. Baker, M. Koppitz, and D.-I. Choi, How to move a black hole without excision: gauge conditions for the numerical evolution of a moving puncture, *Phys. Rev.* **D73**, 124011 (2006), [arXiv:gr-qc/0605030](#).
- [37] R. Borges, M. Carmona, B. Costa, and W. S. Don, An improved weighted essentially non-oscillatory scheme for hyperbolic conservation laws, *Journal of Computational Physics* **227**, 3191 (2008).
- [38] J. S. Read, B. D. Lackey, B. J. Owen, and J. L. Friedman, Constraints on a phenomenologically parameterized neutron-star equation of state, *Phys. Rev. D* **79**, 124032 (2009), [arXiv:0812.2163 \[astro-ph\]](#).
- [39] M. Shibata, K. Taniguchi, and K. Uryu, Merger of binary neutron stars with realistic equations of state in full general relativity, *Phys. Rev.* **D71**, 084021 (2005),

- arXiv:gr-qc/0503119.
- [40] A. Bauswein, H.-T. Janka, and R. Oechslin, Testing Approximations of Thermal Effects in Neutron Star Merger Simulations, *Phys.Rev.* **D82**, 084043 (2010), arXiv:1006.3315 [astro-ph.SR].
- [41] F. Douchin and P. Haensel, A unified equation of state of dense matter and neutron star structure, *Astron. Astrophys.* **380**, 151 (2001), arXiv:astro-ph/0111092.
- [42] M. Alford, M. Braby, M. W. Paris, and S. Reddy, Hybrid stars that masquerade as neutron stars, *Astrophys. J.* **629**, 969 (2005), arXiv:nucl-th/0411016.
- [43] B. D. Lackey, M. Nayyar, and B. J. Owen, Observational constraints on hyperons in neutron stars, *Phys. Rev. D* **73**, 024021 (2006), arXiv:astro-ph/0507312.
- [44] A. Bauswein, O. Just, H.-T. Janka, and N. Stergioulas, Neutron-star radius constraints from GW170817 and future detections, *Astrophys. J. Lett.* **850**, L34 (2017), arXiv:1710.06843 [astro-ph.HE].
- [45] E. Annala, T. Gorda, A. Kurkela, and A. Vuorinen, Gravitational-wave constraints on the neutron-star-matter Equation of State, *Phys. Rev. Lett.* **120**, 172703 (2018), arXiv:1711.02644 [astro-ph.HE].
- [46] E. R. Most, L. R. Weih, L. Rezzolla, and J. Schaffner-Bielich, New constraints on radii and tidal deformabilities of neutron stars from GW170817, *Phys. Rev. Lett.* **120**, 261103 (2018), arXiv:1803.00549 [gr-qc].
- [47] B. P. Abbott *et al.* (LIGO Scientific, Virgo), GW170817: Measurements of neutron star radii and equation of state, *Phys. Rev. Lett.* **121**, 161101 (2018), arXiv:1805.11581 [gr-qc].
- [48] D. Radice and L. Dai, Multimessenger Parameter Estimation of GW170817, *Eur. Phys. J. A* **55**, 50 (2019), arXiv:1810.12917 [astro-ph.HE].
- [49] C. D. Capano, I. Tews, S. M. Brown, B. Margalit, S. De, S. Kumar, D. A. Brown, B. Krishnan, and S. Reddy, Stringent constraints on neutron-star radii from multimessenger observations and nuclear theory, *Nature Astron.* **4**, 625 (2020), arXiv:1908.10352 [astro-ph.HE].
- [50] T. Dietrich, M. W. Coughlin, P. T. H. Pang, M. Bulla, J. Heinzl, L. Issa, I. Tews, and S. Antier, Multimessenger constraints on the neutron-star equation of state and the Hubble constant, *Science* **370**, 1450 (2020), arXiv:2002.11355 [astro-ph.HE].
- [51] I. Legred, K. Chatziioannou, R. Essick, S. Han, and P. Landry, Impact of the PSR J0740+6620 radius constraint on the properties of high-density matter (2021), arXiv:2106.05313 [astro-ph.HE].
- [52] M. C. Miller *et al.*, The Radius of PSR J0740+6620 from NICER and XMM-Newton Data (2021), arXiv:2105.06979 [astro-ph.HE].
- [53] G. Raaijmakers, S. K. Greif, K. Hebeler, T. Hinderer, S. Nissanke, A. Schwenk, T. E. Riley, A. L. Watts, J. M. Lattimer, and W. C. G. Ho, Constraints on the dense matter equation of state and neutron star properties from NICER's mass-radius estimate of PSR J0740+6620 and multimessenger observations (2021), arXiv:2105.06981 [astro-ph.HE].
- [54] S. Huth *et al.*, Constraining Neutron-Star Matter with Microscopic and Macroscopic Collisions (2021), arXiv:2107.06229 [nucl-th].
- [55] I. Tews, J. Carlson, S. Gandolfi, and S. Reddy, Constraining the speed of sound inside neutron stars with chiral effective field theory interactions and observations, *Astrophys. J.* **860**, 149 (2018), arXiv:1801.01923 [nucl-th].
- [56] J. Antoniadis, P. C. Freire, N. Wex, T. M. Tauris, R. S. Lynch, *et al.*, A Massive Pulsar in a Compact Relativistic Binary, *Science* **340**, 6131 (2013), arXiv:1304.6875 [astro-ph.HE].
- [57] Z. Arzoumanian *et al.* (NANOGrav), The NANOGrav 11-year Data Set: High-precision timing of 45 Millisecond Pulsars, *Astrophys. J. Suppl.* **235**, 37 (2018), arXiv:1801.01837 [astro-ph.HE].
- [58] E. Fonseca *et al.*, Refined Mass and Geometric Measurements of the High-mass PSR J0740+6620, *Astrophys. J. Lett.* **915**, L12 (2021), arXiv:2104.00880 [astro-ph.HE].
- [59] B. Margalit and B. D. Metzger, Constraining the Maximum Mass of Neutron Stars From Multi-Messenger Observations of GW170817, *Astrophys. J. Lett.* **850**, L19 (2017), arXiv:1710.05938 [astro-ph.HE].
- [60] L. Rezzolla, E. R. Most, and L. R. Weih, Using gravitational-wave observations and quasi-universal relations to constrain the maximum mass of neutron stars, *Astrophys. J. Lett.* **852**, L25 (2018), arXiv:1711.00314 [astro-ph.HE].
- [61] M. Ruiz, S. L. Shapiro, and A. Tsokaros, GW170817, General Relativistic Magnetohydrodynamic Simulations, and the Neutron Star Maximum Mass, *Phys. Rev. D* **97**, 021501 (2018), arXiv:1711.00473 [astro-ph.HE].
- [62] M. Shibata, S. Fujibayashi, K. Hotokezaka, K. Kiuchi, K. Kyutoku, Y. Sekiguchi, and M. Tanaka, Modeling GW170817 based on numerical relativity and its implications, *Phys. Rev. D* **96**, 123012 (2017), arXiv:1710.07579 [astro-ph.HE].
- [63] M. W. Coughlin, T. Dietrich, B. Margalit, and B. D. Metzger, Multimessenger Bayesian parameter inference of a binary neutron star merger, *Mon. Not. Roy. Astron. Soc.* **489**, L91 (2019), arXiv:1812.04803 [astro-ph.HE].
- [64] M. W. Coughlin *et al.*, Constraints on the neutron star equation of state from AT2017gfo using radiative transfer simulations, *Mon. Not. Roy. Astron. Soc.* **480**, 3871 (2018), arXiv:1805.09371 [astro-ph.HE].
- [65] M. C. Miller *et al.*, PSR J0030+0451 Mass and Radius from NICER Data and Implications for the Properties of Neutron Star Matter, *Astrophys. J. Lett.* **887**, L24 (2019), arXiv:1912.05705 [astro-ph.HE].
- [66] T. E. Riley *et al.*, A NICER View of PSR J0030+0451: Millisecond Pulsar Parameter Estimation, *Astrophys. J. Lett.* **887**, L21 (2019), arXiv:1912.05702 [astro-ph.HE].
- [67] T. E. Riley *et al.*, A NICER View of the Massive Pulsar PSR J0740+6620 Informed by Radio Timing and XMM-Newton Spectroscopy (2021), arXiv:2105.06980 [astro-ph.HE].
- [68] P. Danielewicz, R. Lacey, and W. G. Lynch, Determination of the equation of state of dense matter, *Science* **298**, 1592 (2002), arXiv:nucl-th/0208016.
- [69] P. Russotto *et al.*, Results of the ASY-EOS experiment at GSI: The symmetry energy at suprasaturation density, *Phys. Rev. C* **94**, 034608 (2016), arXiv:1608.04332 [nucl-ex].
- [70] T. Hinderer, Tidal Love numbers of neutron stars, *Astrophys. J.* **677**, 1216 (2008), arXiv:0711.2420 [astro-ph].
- [71] T. Damour and A. Nagar, Relativistic tidal properties of neutron stars, *Phys. Rev. D* **80**, 084035 (2009), arXiv:0906.0096 [gr-qc].
- [72] T. Binnington and E. Poisson, Relativistic theory of tidal Love numbers, *Phys. Rev. D* **80**, 084018 (2009), arXiv:0906.1366 [gr-qc].
- [73] S. Bernuzzi and A. Nagar, Gravitational waves from

- pulsations of neutron stars described by realistic Equations of State, *Phys. Rev.* **D78**, 024024 (2008), [arXiv:0803.3804 \[gr-qc\]](#).
- [74] T. Dietrich, M. Ujevic, W. Tichy, S. Bernuzzi, and B. Brügmann, Gravitational waves and mass ejecta from binary neutron star mergers: Effect of the mass-ratio, *Phys. Rev.* **D95**, 024029 (2017), [arXiv:1607.06636 \[gr-qc\]](#).
- [75] R. Kashyap, A. Das, D. Radice, S. Padamata, A. Prakash, D. Logoteta, A. Perego, D. A. Godzieba, S. Bernuzzi, I. Bombaci, F. J. Fattoyev, B. T. Reed, and A. da Silva Schneider, Numerical relativity simulations of prompt collapse mergers: threshold mass and phenomenological constraints on neutron star properties after gw170817 (2021), [arXiv:2111.05183 \[astro-ph.HE\]](#).
- [76] D. Radice, A. Perego, S. Bernuzzi, and B. Zhang, Long-lived Remnants from Binary Neutron Star Mergers, *Mon. Not. Roy. Astron. Soc.* **481**, 3670 (2018), [arXiv:1803.10865 \[astro-ph.HE\]](#).
- [77] A. Bauswein, S. Blacker, V. Vijayan, N. Stergioulas, K. Chatziioannou, J. A. Clark, N.-U. F. Bastian, D. B. Blaschke, M. Cierniak, and T. Fischer, Equation of state constraints from the threshold binary mass for prompt collapse of neutron star mergers, *Physical Review Letters* **125**, [10.1103/physrevlett.125.141103](#) (2020).
- [78] T. Dietrich, D. Radice, S. Bernuzzi, F. Zappa, A. Perego, B. Brügmann, S. V. Chaurasia, R. Dudi, W. Tichy, and M. Ujevic, CoRe database of binary neutron star merger waveforms, *Class. Quant. Grav.* **35**, 24LT01 (2018), [arXiv:1806.01625 \[gr-qc\]](#).
- [79] K. Hotokezaka, K. Kiuchi, K. Kyutoku, H. Okawa, Y.-i. Sekiguchi, M. Shibata, and K. Taniguchi, Mass ejection from the merger of binary neutron stars, *Phys. Rev. D* **87**, 024001 (2013), [arXiv:1212.0905 \[astro-ph.HE\]](#).
- [80] T. Dietrich and M. Ujevic, Modeling dynamical ejecta from binary neutron star mergers and implications for electromagnetic counterparts, *Class. Quant. Grav.* **34**, 105014 (2017), [arXiv:1612.03665 \[gr-qc\]](#).
- [81] V. Nedora, S. Bernuzzi, D. Radice, B. Daszuta, A. En-drizzi, A. Perego, A. Prakash, M. Safarzadeh, F. Schi-anchi, and D. Logoteta, Numerical Relativity Simulations of the Neutron Star Merger GW170817: Long-Term Remnant Evolutions, Winds, Remnant Disks, and Nucleosynthesis, *Astrophys. J.* **906**, 98 (2021), [arXiv:2008.04333 \[astro-ph.HE\]](#).
- [82] D. Radice, A. Perego, K. Hotokezaka, S. A. Fromm, S. Bernuzzi, and L. F. Roberts, Binary Neutron Star Mergers: Mass Ejection, Electromagnetic Counterparts and Nucleosynthesis, *Astrophys. J.* **869**, 130 (2018), [arXiv:1809.11161 \[astro-ph.HE\]](#).
- [83] S. Bernuzzi *et al.*, Accretion-induced prompt black hole formation in asymmetric neutron star mergers, dynamical ejecta and kilonova signals, *Mon. Not. Roy. Astron. Soc.* **497**, 1488 (2020), [arXiv:2003.06015 \[astro-ph.HE\]](#).

Appendix A: Fits

TABLE VIII. Results for coefficients c_1 to c_5 : fitting threshold mass data (sample K: 21 data points as reported in Tab. IV) for three pairs of stellar parameters (X, Y) to $M_{\text{thr}}(q, X, Y) = c_1 X + c_2 Y + c_3 + c_4 \delta\tilde{q}^3 X + c_5 \delta\tilde{q}^3 Y$, $\delta\tilde{q} = 1 - \tilde{q}$ by means of a least squares approach. Combined fits are given for $Y \in \{R_{1.6}, \Lambda_{1.4}\}$ based on the sample n and the data of Bauswein et al. presented in Tab. IX of [16]. In columns seven to nine we present the following measures of variation: the maximal absolute residual (max.), the mean absolute residual (av.), and the coefficient of determination (R^2).

$M_{\text{thr}}(q, M_{\text{max}}, R_{1.6}) = c_1 M_{\text{max}} + c_2 R_{1.6} + c_3 + c_4 \delta\tilde{q}^3 M_{\text{max}} + c_5 \delta\tilde{q}^3 R_{1.6}$									
sample	c_1	c_2	c_3	c_4	c_5	max.	av.	R^2	N
K	-0.404 ± 0.058	0.105 ± 0.002	2.458 ± 0.1	3.211 ± 0.226	-0.674 ± 0.035	0.069	0.0113	0.9649	21
K+b+e+h	0.675 ± 0.559	0.15 ± 0.106	-0.316 ± 1.191	5.306 ± 25.98	-1.03 ± 4.371	0.148	0.0364	0.9602	141
$M_{\text{thr}}(q, M_{\text{max}}, R_{\text{max}}) = c_1 M_{\text{max}} + c_2 R_{\text{max}} + c_3 + c_4 \delta\tilde{q}^3 M_{\text{max}} + c_5 \delta\tilde{q}^3 R_{\text{max}}$									
K	0.862 ± 0.041	0.164 ± 0.004	-0.602 ± 0.068	4.145 ± 0.282	-0.938 ± 0.05	0.047	0.0105	0.9765	21
$M_{\text{thr}}(q, M_{\text{max}}, \Lambda_{1.4}) = c_1 M_{\text{max}} + c_2 \Lambda_{1.4} + c_3 + c_4 \delta\tilde{q}^3 M_{\text{max}} + c_5 \delta\tilde{q}^3 \Lambda_{1.4}$									
K	-0.382 ± 0.062	3.723 ± 0.076	3.502 ± 0.12	-0.166 ± 0.057	-2.497 ± 0.136	0.074	0.0132	0.9565	21
K+b+e+h	0.67 ± 0.495	5.341 ± 4.097	1.271 ± 0.986	-0.042 ± 5.759	-3.341 ± 19.33	0.131	0.0455	0.9512	141

TABLE IX. Results for coefficients c_1 to c_7 fitting threshold mass data (21 data points as reported in Tab. IV) for four pairs of stellar parameters (X, Y) to $M_{\text{thr}}(q, X, Y) = c_1 X + c_2 Y + c_3 + c_4 \delta\tilde{q} X + c_5 \delta\tilde{q} Y + c_6 \delta\tilde{q}^3 X + c_7 \delta\tilde{q}^3 Y$, $\delta\tilde{q} = 1 - \tilde{q}$ by means of a least squares approach. The following measures of variation are given: the maximal absolute residual (max.), the mean absolute residual (av.), and the coefficient of determination, (R^2).

(X, Y)	$(M_{\text{max}}, R_{1.6})$	$(M_{\text{max}}, R_{\text{max}})$	$(M_{\text{max}}, \Lambda_{1.4})$	$(M_{\text{max}}, \hat{M}_{\text{thr}}(q=1))$
c_1	-0.651 ± 0.021	0.832 ± 0.021	-0.485 ± 0.019	$(5.596 \pm 2.169) \cdot 10^{-2}$
c_2	0.127 ± 0.001	0.19 ± 0.001	$(4.425 \pm 0.039) \cdot 10^{-4}$	0.999 ± 0.008
c_3	2.669 ± 0.039	-0.842 ± 0.045	3.652 ± 0.039	-0.111 ± 0.043
c_4	0.357 ± 0.059	0.766 ± 0.066	$(9.929 \pm 1.309) \cdot 10^{-2}$	1.004 ± 0.094
c_5	$(-4.517 \pm 0.919) \cdot 10^{-2}$	-0.127 ± 0.012	$(-8.172 \pm 3.351) \cdot 10^{-5}$	-0.637 ± 0.063
c_6	3.423 ± 0.302	1.467 ± 0.323	-0.303 ± 0.065	3.276 ± 0.468
c_7	-0.762 ± 0.047	-0.501 ± 0.058	$(-3.194 \pm 0.176) \cdot 10^{-3}$	-3.129 ± 0.316
max.	0.0375	0.0330	0.0371	0.0342
av.	0.0107	0.0079	0.0127	0.0080
R^2	0.9795	0.9866	0.9725	0.9862

TABLE X. Same as Tab. IX, but for a set (K+P) of 57 threshold mass data points; (K, 21 data points) together with data from Ref. [17] (P, 36 data points). The best fit is achieved for the parameter pair $(X, Y) = (M_{\text{max}}, \hat{M}_{\text{thr}}(q=1))$.

(X, Y)	$(M_{\text{max}}, R_{1.6})$	$(M_{\text{max}}, R_{\text{max}})$	$(M_{\text{max}}, \Lambda_{1.4})$	$(M_{\text{max}}, \hat{M}_{\text{thr}}(q=1))$
c_1	0.463 ± 0.094	-0.137 ± 0.642	$(-1.525 \pm 2.481) \cdot 10^{-3}$	$(-3.667 \pm 8.928) \cdot 10^{-2}$
c_2	0.141 ± 0.016	-0.403 ± 3.414	-0.769 ± 0.738	0.932 ± 0.064
c_3	0.246 ± 0.107	-0.156 ± 0.117	$(-3.738 \pm 4.635) \cdot 10^{-4}$	0.281 ± 0.067
c_4	0.735 ± 0.639	0.8670 ± 0.623	0.156 ± 0.137	1.11 ± 0.626
c_5	-0.116 ± 0.106	-0.156 ± 0.117	$(-3.738 \pm 4.635) \cdot 10^{-4}$	-0.753 ± 0.44
c_6	0.172 ± 3.456	-0.403 ± 3.414	-0.769 ± 0.738	1.191 ± 3.357
c_7	-0.214 ± 0.574	-0.137 ± 0.642	$(-1.525 \pm 2.481) \cdot 10^{-3}$	-1.625 ± 2.355
max.	0.0846	0.0851	0.0802	0.0708
av.	0.0289	0.0343	0.0305	0.0181
R^2	0.9382	0.9258	0.9339	0.9741

Appendix B: Configurations

TABLE XI. BNS configurations with EOS SLy. Mass ratio q and total mass M (columns two and three) directly determine the gravitational masses, M_1 and M_2 , of the stars (columns four and five). The chirp mass \mathcal{M} of the binary is given in column six. The baryonic masses, M_1^b and M_2^b (columns seven and eight), as well as the radii, R_1 and R_2 (columns nine and ten), of the individual stars are provided by SGRID. The stars' compactnesses, C_1 and C_2 (columns eleven and twelve), are calculated as $C_i = (GM_i)/(c^2 R_i)$. The tidal polarizability quantities, $\Lambda_2^{(1)}$, $\Lambda_2^{(2)}$, $\tilde{\Lambda}$ and κ_2^T (columns thirteen to sixteen), are calculated using formulas (3) to (5).

EOS	q	M [M_\odot]	M_1 [M_\odot]	M_2 [M_\odot]	\mathcal{M} [M_\odot]	M_1^b [M_\odot]	M_2^b [M_\odot]	R_1 [km]	R_2 [km]	C_1	C_2	$\Lambda_2^{(1)}$	$\Lambda_2^{(2)}$	$\tilde{\Lambda}$	κ_2^T
SLy	1.000	2.70	1.350	1.350	1.175	1.495	1.495	11.47	11.47	0.1738	0.1738	389	389	389	36.5
SLy	1.000	2.75	1.375	1.375	1.197	1.526	1.526	11.47	11.47	0.1771	0.1771	345	345	345	32.3
SLy	1.000	2.80	1.400	1.400	1.219	1.557	1.557	11.46	11.46	0.1804	0.1804	307	307	307	28.8
SLy	1.000	2.85	1.425	1.425	1.241	1.588	1.588	11.46	11.46	0.1837	0.1837	272	272	272	25.5
SLy	1.000	2.90	1.450	1.450	1.262	1.620	1.620	11.45	11.45	0.1870	0.1870	242	242	242	22.7
SLy	1.000	3.00	1.500	1.500	1.306	1.683	1.683	11.43	11.43	0.1938	0.1938	191	191	191	17.9
SLy	1.000	3.10	1.550	1.550	1.349	1.747	1.747	11.41	11.41	0.2007	0.2007	151	151	151	14.1
SLy	1.125	2.75	1.456	1.294	1.195	1.627	1.426	11.45	11.48	0.1878	0.1665	235	511	351	32.9
SLy	1.125	2.80	1.482	1.318	1.216	1.661	1.455	11.44	11.48	0.1914	0.1696	207	455	311	29.2
SLy	1.125	2.85	1.509	1.341	1.238	1.695	1.484	11.43	11.47	0.1950	0.1726	183	405	276	25.9
SLy	1.125	2.90	1.535	1.365	1.260	1.729	1.513	11.42	11.47	0.1986	0.1757	161	363	246	23.1
SLy	1.125	3.00	1.588	1.412	1.303	1.797	1.572	11.38	11.46	0.2060	0.1819	125	290	194	18.2
SLy	1.125	3.10	1.641	1.459	1.347	1.867	1.631	11.35	11.45	0.2136	0.1882	97	233	154	14.4
SLy	1.250	2.70	1.500	1.200	1.167	1.683	1.312	11.43	11.47	0.1938	0.1545	191	813	409	38.5
SLy	1.250	2.75	1.528	1.222	1.188	1.719	1.338	11.42	11.48	0.1976	0.1573	167	727	364	34.3
SLy	1.250	2.80	1.556	1.244	1.210	1.755	1.365	11.40	11.48	0.2015	0.1601	147	651	323	30.5
SLy	1.250	2.85	1.583	1.267	1.231	1.791	1.392	11.39	11.48	0.2054	0.1630	128	583	288	27.1
SLy	1.250	2.90	1.611	1.289	1.253	1.827	1.419	11.37	11.48	0.2093	0.1659	112	523	256	24.1
SLy	1.250	3.00	1.667	1.333	1.296	1.900	1.474	11.32	11.48	0.2174	0.1716	86	422	203	19.2
SLy	1.250	3.10	1.722	1.378	1.339	1.975	1.529	11.27	11.47	0.2257	0.1774	65	341	161	15.2
SLy	1.375	2.75	1.592	1.158	1.179	1.802	1.261	11.38	11.47	0.2066	0.1491	123	999	381	36.0
SLy	1.375	2.80	1.621	1.179	1.200	1.840	1.286	11.36	11.47	0.2107	0.1518	107	901	340	32.2
SLy	1.375	2.85	1.650	1.200	1.222	1.878	1.312	11.34	11.47	0.2149	0.1545	93	813	304	28.8
SLy	1.375	2.90	1.679	1.221	1.243	1.917	1.337	11.31	11.48	0.2192	0.1572	81	731	271	25.7
SLy	1.375	3.00	1.737	1.263	1.286	1.995	1.388	11.25	11.48	0.2280	0.1625	60	594	216	20.5
SLy	1.375	3.10	1.795	1.305	1.329	2.074	1.439	11.17	11.48	0.2372	0.1680	45	484	173	16.4
SLy	1.500	2.70	1.620	1.080	1.147	1.839	1.169	11.36	11.45	0.2106	0.1393	108	1,499	452	42.9
SLy	1.500	2.75	1.650	1.100	1.168	1.878	1.192	11.34	11.45	0.2149	0.1418	93	1,349	403	38.3
SLy	1.500	2.80	1.680	1.120	1.189	1.918	1.216	11.31	11.46	0.2194	0.1444	80	1,218	361	34.3
SLy	1.500	2.85	1.710	1.140	1.211	1.958	1.240	11.28	11.46	0.2239	0.1469	69	1,101	323	30.7
SLy	1.500	2.90	1.740	1.160	1.232	1.999	1.264	11.25	11.47	0.2285	0.1494	59	993	289	27.5
SLy	1.500	3.00	1.800	1.200	1.274	2.081	1.312	11.17	11.47	0.2381	0.1545	43	813	232	22.1
SLy	1.500	3.10	1.860	1.240	1.317	2.165	1.360	11.06	11.48	0.2484	0.1596	31	666	186	17.7
SLy	1.625	2.75	1.702	1.048	1.156	1.948	1.131	11.29	11.44	0.2227	0.1353	72	1,784	429	40.9
SLy	1.625	2.80	1.733	1.067	1.177	1.990	1.153	11.26	11.45	0.2275	0.1377	61	1,601	382	36.5
SLy	1.625	2.85	1.764	1.086	1.198	2.032	1.176	11.22	11.45	0.2323	0.1400	52	1,453	343	32.8
SLy	1.625	2.90	1.795	1.105	1.219	2.074	1.198	11.17	11.46	0.2373	0.1424	44	1,321	309	29.6
SLy	1.625	3.00	1.857	1.143	1.261	2.161	1.243	11.07	11.46	0.2479	0.1472	31	1,083	249	23.8
SLy	1.625	3.10	1.919	1.181	1.303	2.249	1.289	10.92	11.47	0.2595	0.1521	22	893	201	19.3
SLy	1.750	2.70	1.750	1.000	1.143	2.013	1.075	11.24	11.42	0.2301	0.1293	56	2,311	499	47.8
SLy	1.750	2.75	1.750	1.000	1.143	2.013	1.075	11.24	11.42	0.2301	0.1293	56	2,311	455	43.6
SLy	1.750	2.80	1.782	1.018	1.164	2.056	1.096	11.19	11.43	0.2351	0.1316	48	2,150	418	40.1
SLy	1.750	2.85	1.814	1.036	1.184	2.100	1.118	11.14	11.44	0.2404	0.1339	40	1,896	367	35.2
SLy	1.750	2.90	1.845	1.055	1.205	2.144	1.139	11.09	11.44	0.2458	0.1361	34	1,720	330	31.7
SLy	1.750	3.00	1.909	1.091	1.247	2.235	1.182	10.95	11.45	0.2576	0.1407	23	1,418	267	25.7
SLy	1.750	3.10	1.973	1.127	1.288	2.327	1.225	10.75	11.46	0.2711	0.1453	15	1,173	217	20.9

TABLE XII. Same as Tab. XI, but for EOS ALF2.

EOS	q	M [M_{\odot}]	M_1 [M_{\odot}]	M_2 [M_{\odot}]	\mathcal{M} [M_{\odot}]	M_1^b [M_{\odot}]	M_2^b [M_{\odot}]	R_1 [km]	R_2 [km]	C_1	C_2	$\Lambda_2^{(1)}$	$\Lambda_2^{(2)}$	$\tilde{\Lambda}$	κ_2^T
ALF2	1.0000	2.80	1.400	1.400	1.219	1.549	1.549	12.39	12.39	0.1669	0.1669	589	589	589	55.3
ALF2	1.0000	2.85	1.425	1.425	1.241	1.579	1.579	12.40	12.40	0.1697	0.1697	529	529	529	49.6
ALF2	1.0000	2.90	1.450	1.450	1.262	1.610	1.610	12.41	12.41	0.1726	0.1726	475	475	475	44.5
ALF2	1.0000	2.95	1.475	1.475	1.284	1.641	1.641	12.41	12.41	0.1755	0.1755	427	427	427	40.0
ALF2	1.0000	3.00	1.500	1.500	1.306	1.672	1.672	12.42	12.42	0.1784	0.1784	381	381	381	35.8
ALF2	1.0000	3.10	1.550	1.550	1.349	1.735	1.735	12.42	12.42	0.1844	0.1844	307	307	307	28.8
ALF2	1.0000	3.20	1.600	1.600	1.393	1.798	1.798	12.41	12.41	0.1904	0.1904	246	246	246	23.1
ALF2	1.1250	2.80	1.482	1.318	1.216	1.650	1.448	12.42	12.34	0.1763	0.1577	414	843	594	55.8
ALF2	1.1250	2.85	1.509	1.341	1.238	1.683	1.477	12.42	12.36	0.1794	0.1603	367	760	532	50.0
ALF2	1.1250	2.90	1.535	1.365	1.260	1.716	1.506	12.42	12.37	0.1826	0.1629	328	687	479	45.0
ALF2	1.1250	2.95	1.562	1.388	1.281	1.750	1.534	12.42	12.38	0.1858	0.1656	292	621	430	40.3
ALF2	1.1250	3.00	1.588	1.412	1.303	1.783	1.563	12.41	12.39	0.1890	0.1682	259	560	385	36.2
ALF2	1.1250	3.10	1.641	1.459	1.347	1.851	1.621	12.39	12.41	0.1956	0.1736	204	458	310	29.1
ALF2	1.1250	3.20	1.694	1.506	1.390	1.919	1.680	12.36	12.42	0.2024	0.1791	159	372	248	23.3
ALF2	1.2500	2.80	1.556	1.244	1.210	1.742	1.361	12.42	12.28	0.1850	0.1497	300	1,155	601	56.6
ALF2	1.2500	2.85	1.583	1.267	1.231	1.777	1.387	12.41	12.30	0.1884	0.1521	265	1,054	543	51.1
ALF2	1.2500	2.90	1.611	1.289	1.253	1.812	1.414	12.41	12.32	0.1918	0.1545	234	954	487	45.9
ALF2	1.2500	2.95	1.639	1.311	1.275	1.848	1.441	12.40	12.34	0.1953	0.1570	206	868	439	41.3
ALF2	1.2500	3.00	1.667	1.333	1.296	1.884	1.468	12.38	12.35	0.1988	0.1594	181	786	394	37.1
ALF2	1.2500	3.10	1.722	1.378	1.339	1.956	1.522	12.34	12.38	0.2062	0.1644	140	650	319	30.0
ALF2	1.2500	3.20	1.778	1.422	1.383	2.028	1.576	12.28	12.40	0.2138	0.1694	106	536	257	24.2
ALF2	1.3125	2.80	1.589	1.211	1.205	1.784	1.320	12.41	12.25	0.1891	0.1460	258	1,344	609	57.4
ALF2	1.3750	2.80	1.621	1.179	1.200	1.825	1.283	12.40	12.21	0.1930	0.1426	223	1,547	615	58.0
ALF2	1.3750	2.85	1.650	1.200	1.222	1.862	1.308	12.39	12.24	0.1967	0.1448	196	1,413	555	52.5
ALF2	1.3750	2.90	1.679	1.221	1.243	1.899	1.333	12.37	12.26	0.2004	0.1471	171	1,284	499	47.2
ALF2	1.3750	2.95	1.708	1.242	1.265	1.937	1.358	12.35	12.28	0.2042	0.1494	150	1,167	449	42.5
ALF2	1.3750	3.00	1.737	1.263	1.286	1.975	1.383	12.33	12.30	0.2081	0.1517	130	1,068	406	38.4
ALF2	1.3750	3.10	1.795	1.305	1.329	2.051	1.434	12.26	12.33	0.2163	0.1563	98	889	329	31.2
ALF2	1.3750	3.20	1.853	1.347	1.372	2.128	1.485	12.16	12.36	0.2250	0.1610	72	741	267	25.3
ALF2	1.4375	2.80	1.651	1.149	1.195	1.864	1.247	12.39	12.18	0.1969	0.1393	195	1,770	622	58.9
ALF2	1.5000	2.80	1.680	1.120	1.189	1.901	1.213	12.37	12.14	0.2006	0.1362	170	2,016	630	59.7
ALF2	1.5000	2.85	1.710	1.140	1.211	1.940	1.237	12.35	12.17	0.2045	0.1384	148	1,841	568	53.9
ALF2	1.5000	2.90	1.740	1.160	1.232	1.979	1.260	12.32	12.19	0.2086	0.1405	128	1,687	514	48.8
ALF2	1.5000	2.95	1.770	1.180	1.253	2.018	1.284	12.29	12.21	0.2127	0.1427	111	1,543	465	44.1
ALF2	1.5000	3.00	1.800	1.200	1.274	2.058	1.308	12.25	12.24	0.2170	0.1448	95	1,413	420	39.9
ALF2	1.5000	3.10	1.860	1.240	1.317	2.138	1.355	12.15	12.28	0.2262	0.1492	69	1,178	342	32.5
ALF2	1.5000	3.20	1.920	1.280	1.359	2.220	1.403	11.99	12.31	0.2365	0.1536	48	993	279	26.6
ALF2	1.5625	2.80	1.707	1.093	1.183	1.936	1.181	12.35	12.11	0.2042	0.1333	150	2,279	636	60.5
ALF2	1.6250	2.70	1.671	1.029	1.135	1.890	1.107	12.38	12.02	0.1994	0.1264	177	3,073	788	74.9
ALF2	1.6250	2.75	1.702	1.048	1.156	1.930	1.129	12.36	12.05	0.2035	0.1285	154	2,815	714	67.9
ALF2	1.6250	2.80	1.733	1.067	1.177	1.970	1.151	12.33	12.07	0.2077	0.1305	133	2,551	641	61.0
ALF2	1.6250	2.85	1.764	1.086	1.198	2.011	1.173	12.30	12.10	0.2119	0.1325	114	2,355	584	55.6
ALF2	1.6250	2.90	1.795	1.105	1.219	2.052	1.195	12.26	12.12	0.2163	0.1346	97	2,160	529	50.4
ALF2	1.6250	2.95	1.826	1.124	1.240	2.093	1.218	12.21	12.15	0.2209	0.1366	83	1,979	478	45.7
ALF2	1.6250	3.00	1.857	1.143	1.261	2.134	1.240	12.15	12.17	0.2257	0.1387	70	1,818	434	41.4
ALF2	1.6250	3.10	1.919	1.181	1.303	2.219	1.285	11.99	12.22	0.2364	0.1428	48	1,537	356	34.1
ALF2	1.6250	3.20	1.981	1.219	1.345	2.305	1.330	11.61	12.26	0.2520	0.1469	27	1,295	287	27.6
ALF2	1.7500	2.70	1.718	0.982	1.122	1.950	1.053	12.34	11.95	0.2056	0.1214	143	3,845	806	76.9
ALF2	1.7500	2.75	1.750	1.000	1.143	1.992	1.074	12.31	11.98	0.2099	0.1233	122	3,529	731	69.8
ALF2	1.7500	2.80	1.782	1.018	1.164	2.034	1.095	12.27	12.00	0.2144	0.1253	104	3,237	663	63.4
ALF2	1.7500	2.85	1.814	1.036	1.184	2.076	1.116	12.23	12.03	0.2190	0.1272	89	2,964	600	57.4
ALF2	1.7500	2.90	1.845	1.055	1.205	2.119	1.137	12.18	12.06	0.2239	0.1292	75	2,716	543	52.0
ALF2	1.7500	2.95	1.877	1.073	1.226	2.162	1.158	12.11	12.08	0.2290	0.1311	63	2,509	495	47.5
ALF2	1.7500	3.00	1.909	1.091	1.247	2.205	1.179	12.03	12.11	0.2345	0.1331	51	2,294	447	42.9
ALF2	1.7500	3.10	1.973	1.127	1.288	2.294	1.222	11.70	12.15	0.2490	0.1370	30	1,947	366	35.2

TABLE XIII. Same as Tab. XI, but for EOS H4.

EOS	q	M [M_{\odot}]	M_1 [M_{\odot}]	M_2 [M_{\odot}]	\mathcal{M} [M_{\odot}]	M_1^b [M_{\odot}]	M_2^b [M_{\odot}]	R_1 [km]	R_2 [km]	C_1	C_2	$\Lambda_2^{(1)}$	$\Lambda_2^{(2)}$	$\tilde{\Lambda}$	κ_2^T
H4	1.000	2.80	1.400	1.400	1.219	1.528	1.528	13.56	13.56	0.1525	0.1525	886	886	886	83.0
H4	1.000	2.90	1.450	1.450	1.262	1.589	1.589	13.55	13.55	0.1581	0.1581	707	707	707	66.3
H4	1.000	2.95	1.475	1.475	1.284	1.619	1.619	13.54	13.54	0.1609	0.1609	634	634	634	59.4
H4	1.000	3.00	1.500	1.500	1.306	1.649	1.649	13.53	13.53	0.1638	0.1638	568	568	568	53.3
H4	1.000	3.10	1.550	1.550	1.349	1.711	1.711	13.50	13.50	0.1696	0.1696	452	452	452	42.4
H4	1.000	3.20	1.600	1.600	1.393	1.772	1.772	13.46	13.46	0.1756	0.1756	359	359	359	33.6
H4	1.000	3.30	1.650	1.650	1.436	1.835	1.835	13.40	13.40	0.1818	0.1818	283	283	283	26.6
H4	1.125	2.90	1.535	1.365	1.260	1.693	1.486	13.51	13.56	0.1679	0.1486	483	1,039	716	67.2
H4	1.125	2.95	1.562	1.388	1.281	1.725	1.514	13.49	13.56	0.1710	0.1512	428	935	641	60.1
H4	1.125	3.00	1.588	1.412	1.303	1.758	1.543	13.47	13.56	0.1742	0.1538	378	842	573	53.8
H4	1.125	3.10	1.641	1.459	1.347	1.824	1.599	13.41	13.54	0.1807	0.1591	296	686	459	43.1
H4	1.125	3.20	1.694	1.506	1.390	1.890	1.657	13.35	13.53	0.1875	0.1644	229	551	364	34.2
H4	1.125	3.30	1.747	1.553	1.433	1.958	1.714	13.26	13.50	0.1946	0.1699	176	445	288	27.1
H4	1.250	2.90	1.611	1.289	1.253	1.786	1.396	13.45	13.55	0.1770	0.1405	340	1,459	733	69.0
H4	1.250	2.95	1.639	1.311	1.275	1.821	1.423	13.42	13.56	0.1804	0.1428	299	1,320	657	61.9
H4	1.250	3.00	1.667	1.333	1.296	1.856	1.449	13.38	13.56	0.1839	0.1452	262	1,195	589	55.5
H4	1.250	3.10	1.722	1.378	1.339	1.926	1.502	13.30	13.56	0.1912	0.1501	200	980	472	44.5
H4	1.250	3.20	1.778	1.422	1.383	1.997	1.555	13.20	13.55	0.1990	0.1550	150	803	378	35.6
H4	1.250	3.30	1.833	1.467	1.426	2.069	1.609	13.06	13.54	0.2073	0.1600	111	658	301	28.4
H4	1.375	2.90	1.679	1.221	1.243	1.871	1.317	13.37	13.53	0.1855	0.1332	247	1,994	761	72.0
H4	1.375	2.95	1.708	1.242	1.265	1.908	1.341	13.32	13.54	0.1893	0.1355	214	1,818	685	64.8
H4	1.375	3.00	1.737	1.263	1.286	1.945	1.366	13.28	13.55	0.1932	0.1377	185	1,642	612	58.0
H4	1.375	3.10	1.795	1.305	1.329	2.019	1.416	13.16	13.56	0.2014	0.1422	137	1,357	494	46.8
H4	1.375	3.20	1.853	1.347	1.372	2.095	1.466	13.01	13.56	0.2104	0.1468	99	1,121	397	37.6
H4	1.375	3.30	1.911	1.389	1.415	2.171	1.516	12.81	13.56	0.2204	0.1514	69	927	318	30.2
H4	1.500	2.90	1.740	1.160	1.232	1.949	1.246	13.27	13.51	0.1937	0.1268	182	2,659	794	75.4
H4	1.500	2.95	1.770	1.180	1.253	1.987	1.269	13.21	13.52	0.1979	0.1289	156	2,411	712	67.7
H4	1.500	3.00	1.800	1.200	1.274	2.026	1.292	13.15	13.53	0.2022	0.1310	133	2,195	640	60.9
H4	1.500	3.10	1.860	1.240	1.317	2.104	1.339	12.98	13.54	0.2116	0.1353	95	1,825	519	49.4
H4	1.500	3.20	1.920	1.280	1.359	2.184	1.386	12.77	13.55	0.2221	0.1395	65	1,521	420	40.1
H4	1.500	3.30	1.980	1.320	1.402	2.265	1.433	12.43	13.56	0.2353	0.1438	40	1,269	338	32.3
H4	1.625	2.80	1.733	1.067	1.177	1.940	1.138	13.28	13.47	0.1927	0.1170	189	4,189	1,026	97.8
H4	1.625	2.85	1.764	1.086	1.198	1.980	1.160	13.22	13.48	0.1970	0.1190	161	3,775	915	87.3
H4	1.625	2.90	1.795	1.105	1.219	2.020	1.182	13.16	13.49	0.2015	0.1210	137	3,465	830	79.2
H4	1.625	2.95	1.826	1.124	1.240	2.060	1.204	13.08	13.50	0.2062	0.1230	115	3,162	748	71.5
H4	1.625	3.00	1.857	1.143	1.261	2.100	1.226	12.99	13.50	0.2111	0.1250	96	2,886	675	64.5
H4	1.625	3.10	1.919	1.181	1.303	2.183	1.270	12.77	13.52	0.2220	0.1290	65	2,398	546	52.4
H4	1.625	3.20	1.981	1.219	1.345	2.267	1.314	12.42	13.53	0.2355	0.1330	40	2,011	444	42.7
H4	1.750	2.80	1.782	1.018	1.164	2.002	1.083	13.19	13.44	0.1996	0.1119	147	5,375	1,074	102.9
H4	1.750	2.85	1.814	1.036	1.184	2.044	1.104	13.11	13.45	0.2043	0.1138	124	4,892	967	92.7
H4	1.750	2.90	1.845	1.055	1.205	2.085	1.125	13.03	13.46	0.2092	0.1157	103	4,459	872	83.7
H4	1.750	2.95	1.877	1.073	1.226	2.127	1.145	12.93	13.47	0.2145	0.1176	85	4,070	787	75.6
H4	1.750	3.00	1.909	1.091	1.247	2.169	1.166	12.81	13.48	0.2201	0.1195	70	3,701	707	68.0
H4	1.750	3.10	1.973	1.127	1.288	2.255	1.208	12.48	13.50	0.2335	0.1234	43	3,112	579	55.8

Appendix C: Results

TABLE XIV. Summary of results - subset: EOS SLy. Columns one to four characterize the simulations in terms of EOS, resolution (res), mass ratio (q) and total mass (M). Residual eccentricities are given in column five. Whether or not a BH was formed within simulation time is answered in column six, in accordance with the merger types reported in column seven, if there is a conclusive answer. If the merger type deviates between resolutions, both of the respective types are reported. Results for the collapse time t_{coll} are given in column seven. In cases where a BH was formed its (gravitational) mass M_{BH} , its spin χ_{BH} , and the (baryonic) mass of the disk M_{disk} , are reported in columns eight to ten.

EOS	res	q	M [M_{\odot}]	ecc [10^{-2}]	BH	Type	t_{coll} [ms]	M_{BH} [M_{\odot}]	χ_{BH}	M_{disk} [$10^{-2} M_{\odot}$]
SLy	R3	1.000	2.70	1.51	no	IV				
SLy	R3, R2	1.000	2.75	$1.50 \pm 0.4\%$	yes	II	2.15 ± 0.10	2.642 ± 0.010	0.708 ± 0.012	2.365 ± 0.4
SLy	R3, R2	1.000	2.80	$1.47 \pm 0.3\%$	yes	I/II	1.28 ± 1.18	2.716 ± 0.040	0.749 ± 0.063	0.159 ± 2.4
SLy	R3, R2	1.000	2.85	$1.53 \pm 3.7\%$	yes	I	0.85 ± 0.01	2.780 ± 0.010	0.768 ± 0.012	0.195 ± 0.1
SLy	R3, R2	1.000	2.90	$1.74 \pm 5.4\%$	yes	I	0.73 ± 0.02	2.831 ± 0.009	0.768 ± 0.009	0.056 ± 0.0
SLy	R3, R2	1.000	3.00	$1.95 \pm 1.2\%$	yes	I	0.63 ± 0.00	2.930 ± 0.003	0.760 ± 0.005	0.007 ± 0.0
SLy	R3, R2	1.000	3.10	$2.00 \pm 0.6\%$	yes	I	0.56 ± 0.00	3.025 ± 0.003	0.750 ± 0.004	0.004 ± 0.0
SLy	R3, R2	1.125	2.75	$1.50 \pm 0.5\%$	yes	III	7.93 ± 5.60	2.541 ± 0.070	0.568 ± 0.064	10.427 ± 6.5
SLy	R3, R2	1.125	2.80	$1.47 \pm 0.5\%$	yes	II/III	6.26 ± 1.31	2.616 ± 0.015	0.613 ± 0.016	8.051 ± 1.1
SLy	R3, R2	1.125	2.85	$1.52 \pm 4.1\%$	yes	I	0.91 ± 0.04	2.766 ± 0.012	0.752 ± 0.014	1.370 ± 0.4
SLy	R3, R2	1.125	2.90	$1.72 \pm 3.2\%$	yes	I	0.78 ± 0.01	2.823 ± 0.007	0.758 ± 0.009	0.904 ± 0.2
SLy	R3, R2	1.125	3.00	$1.94 \pm 1.4\%$	yes	I	0.65 ± 0.00	2.928 ± 0.004	0.757 ± 0.006	0.319 ± 0.0
SLy	R3, R2	1.125	3.10	$1.98 \pm 0.8\%$	yes	I	0.57 ± 0.01	3.025 ± 0.002	0.749 ± 0.004	0.080 ± 0.0
SLy	R3	1.250	2.70	1.54	no	IV				
SLy	R3, R2	1.250	2.75	$1.53 \pm 0.2\%$?	III/IV	14.10	2.483	0.522	16.119
SLy	R3, R2	1.250	2.80	$1.48 \pm 0.2\%$	yes	II/III	15.38 ± 13.05	2.490 ± 0.156	0.506 ± 0.157	21.188 ± 13.7
SLy	R3, R2	1.250	2.85	$1.49 \pm 3.7\%$	yes	I	1.04 ± 0.04	2.710 ± 0.009	0.693 ± 0.009	7.292 ± 0.5
SLy	R3, R2	1.250	2.90	$1.69 \pm 3.2\%$	yes	I	0.85 ± 0.03	2.784 ± 0.005	0.717 ± 0.006	5.346 ± 0.2
SLy	R3, R2	1.250	3.00	$1.94 \pm 1.1\%$	yes	I	0.66 ± 0.02	2.915 ± 0.005	0.743 ± 0.006	2.057 ± 0.3
SLy	R3, R2	1.250	3.10	$1.98 \pm 0.7\%$	yes	I	0.58 ± 0.01	3.022 ± 0.003	0.745 ± 0.004	0.936 ± 0.1
SLy	R3, R2	1.375	2.75	$1.54 \pm 0.5\%$	yes	III	9.84 ± 13.25	2.482 ± 0.051	0.516 ± 0.051	18.503 ± 4.8
SLy	R3, R2	1.375	2.80	$1.49 \pm 0.2\%$	yes	II	2.40 ± 0.27	2.639 ± 0.003	0.653 ± 0.001	9.594 ± 0.3
SLy	R3, R2	1.375	2.85	$1.47 \pm 3.3\%$	yes	I	1.05 ± 0.05	2.691 ± 0.009	0.666 ± 0.011	10.582 ± 1.0
SLy	R3, R2	1.375	2.90	$1.66 \pm 3.6\%$	yes	I	0.85 ± 0.04	2.760 ± 0.004	0.687 ± 0.004	8.364 ± 0.3
SLy	R3, R2	1.375	3.00	$1.92 \pm 1.6\%$	yes	I	0.68 ± 0.02	2.884 ± 0.006	0.708 ± 0.008	5.997 ± 0.5
SLy	R3, R2	1.375	3.10	$2.00 \pm 0.5\%$	yes	I	0.58 ± 0.01	2.994 ± 0.005	0.715 ± 0.006	4.614 ± 0.4
SLy	R3	1.500	2.70	1.54	no	IV				
SLy	R3, R2	1.500	2.75	$1.53 \pm 0.1\%$?	III/IV	24.05	2.442	0.474	24.423
SLy	R3, R2	1.500	2.80	$1.50 \pm 0.1\%$	yes	I	1.44 ± 0.10	2.622 ± 0.002	0.632 ± 0.004	13.055 ± 0.2
SLy	R3, R2	1.500	2.85	$1.46 \pm 1.7\%$	yes	I	0.99 ± 0.03	2.677 ± 0.008	0.640 ± 0.009	12.867 ± 0.5
SLy	R3, R2	1.500	2.90	$1.63 \pm 3.8\%$	yes	I	0.85 ± 0.03	2.741 ± 0.007	0.657 ± 0.010	11.454 ± 0.5
SLy	R3, R2	1.500	3.00	$1.96 \pm 1.2\%$	yes	I	0.67 ± 0.02	2.866 ± 0.006	0.681 ± 0.008	8.536 ± 0.4
SLy	R3, R2	1.500	3.10	$2.03 \pm 0.4\%$	yes	I	0.57 ± 0.03	2.968 ± 0.002	0.682 ± 0.004	7.969 ± 0.2
SLy	R3, R2	1.625	2.75	$1.54 \pm 0.5\%$?	II/IV	2.83	2.527	0.566	18.343
SLy	R3, R2	1.625	2.80	$1.52 \pm 0.0\%$	yes	I	1.11 ± 0.01	2.622 ± 0.010	0.618 ± 0.010	13.807 ± 0.8
SLy	R3, R2	1.625	2.85	$1.46 \pm 0.5\%$	yes	I	0.94 ± 0.02	2.670 ± 0.009	0.618 ± 0.010	14.112 ± 0.7
SLy	R3, R2	1.625	2.90	$1.59 \pm 4.4\%$	yes	I	0.81 ± 0.04	2.726 ± 0.005	0.627 ± 0.007	13.531 ± 0.2
SLy	R3, R2	1.625	3.00	$1.96 \pm 1.5\%$	yes	I	0.66 ± 0.01	2.846 ± 0.006	0.648 ± 0.007	11.012 ± 0.6
SLy	R3, R2	1.625	3.10	$2.07 \pm 0.5\%$	yes	I	0.56 ± 0.01	2.946 ± 0.007	0.648 ± 0.007	10.661 ± 0.8
SLy	R3	1.750	2.70	1.54	no	IV				
SLy	R3, R2	1.750	2.75	$1.55 \pm 0.6\%$	yes	I	1.26 ± 0.03	2.560 ± 0.009	0.585 ± 0.011	15.589 ± 0.7
SLy	R3, R2	1.750	2.80	$1.53 \pm 0.2\%$	yes	I	1.02 ± 0.02	2.615 ± 0.008	0.591 ± 0.008	15.036 ± 0.7
SLy	R3, R2	1.750	2.85	$1.47 \pm 0.1\%$	yes	I	0.89 ± 0.01	2.660 ± 0.004	0.591 ± 0.006	15.431 ± 0.4
SLy	R3, R2	1.750	2.90	$1.52 \pm 5.3\%$	yes	I	0.80 ± 0.01	2.712 ± 0.004	0.595 ± 0.004	15.141 ± 0.4
SLy	R3, R2	1.750	3.00	$1.94 \pm 2.5\%$	yes	I	0.63 ± 0.01	2.830 ± 0.002	0.616 ± 0.003	12.992 ± 0.1
SLy	R3, R2	1.750	3.10	$2.09 \pm 1.3\%$	yes	I	0.50 ± 0.01	2.930 ± 0.007	0.618 ± 0.009	12.553 ± 1.1

TABLE XV. Same as Tab. XIV, but for EOS ALF2.

EOS	res	q	M [M_{\odot}]	ecc [10^{-2}]	BH	Type	t_{coll} [ms]	M_{BH} [M_{\odot}]	χ_{BH}	M_{disk} [$10^{-2} M_{\odot}$]
ALF2	R3, R2, R1	1.000	2.80	$1.63 \pm 4.5\%$	yes	III	7.47 ± 1.46	2.652 ± 0.034	0.642 ± 0.035	5.981 ± 3.5
ALF2	R3, R2	1.000	2.85	$1.77 \pm 2.6\%$	yes	II/III	4.76 ± 1.29	2.730 ± 0.020	0.680 ± 0.015	3.259 ± 2.4
ALF2	R3, R2, R1	1.000	2.90	$1.83 \pm 1.5\%$	yes	II	3.41 ± 0.04	2.788 ± 0.005	0.708 ± 0.003	3.189 ± 1.0
ALF2	R3, R2	1.000	2.95	$1.85 \pm 0.9\%$	yes	II	2.25 ± 0.03	2.849 ± 0.003	0.737 ± 0.000	2.456 ± 0.6
ALF2	R3, R2, R1	1.000	3.00	$1.85 \pm 0.9\%$	yes	I/II	1.20 ± 0.46	2.927 ± 0.019	0.776 ± 0.022	0.240 ± 1.3
ALF2	R3, R2, R1	1.000	3.10	$1.83 \pm 0.2\%$	yes	I	0.84 ± 0.02	3.036 ± 0.000	0.786 ± 0.002	0.205 ± 0.0
ALF2	R3, R2	1.000	3.20	$1.72 \pm 0.7\%$	yes	I	0.74 ± 0.01	3.134 ± 0.000	0.778 ± 0.001	0.090 ± 0.0
ALF2	R3, R2	1.125	2.80	$1.59 \pm 5.1\%$	yes	III	10.74 ± 1.52	2.548 ± 0.023	0.558 ± 0.022	18.283 ± 2.6
ALF2	R3, R2	1.125	2.85	$1.75 \pm 2.8\%$	yes	III	5.12 ± 1.01	2.719 ± 0.030	0.680 ± 0.030	5.212 ± 3.2
ALF2	R3, R2	1.125	2.90	$1.82 \pm 1.7\%$	yes	II	3.76 ± 0.13	2.791 ± 0.014	0.710 ± 0.021	2.984 ± 1.2
ALF2	R3, R2	1.125	2.95	$1.87 \pm 1.1\%$	yes	II	2.32 ± 0.02	2.852 ± 0.008	0.739 ± 0.013	2.791 ± 0.3
ALF2	R3, R2	1.125	3.00	$1.89 \pm 0.8\%$	yes	I	1.10 ± 0.15	2.916 ± 0.010	0.765 ± 0.014	2.024 ± 0.4
ALF2	R3, R2	1.125	3.10	$1.86 \pm 0.2\%$	yes	I	0.84 ± 0.02	3.022 ± 0.003	0.771 ± 0.004	1.834 ± 0.4
ALF2	R3, R2	1.125	3.20	$1.73 \pm 1.0\%$	yes	I	0.72 ± 0.02	3.129 ± 0.001	0.772 ± 0.001	0.841 ± 0.1
ALF2	R3, R2, R1	1.250	2.80	$1.55 \pm 5.4\%$	yes	III	9.44 ± 1.17	2.546 ± 0.002	0.555 ± 0.006	18.609 ± 0.1
ALF2	R3, R2	1.250	2.85	$1.73 \pm 3.1\%$	yes	II	4.99 ± 0.31	2.661 ± 0.006	0.624 ± 0.005	11.760 ± 1.3
ALF2	R3, R2, R1	1.250	2.90	$1.84 \pm 1.7\%$	yes	II	3.56 ± 0.14	2.745 ± 0.003	0.653 ± 0.000	7.452 ± 0.7
ALF2	R3, R2	1.250	2.95	$1.89 \pm 0.9\%$	yes	II	2.55 ± 0.14	2.796 ± 0.001	0.671 ± 0.000	7.961 ± 0.3
ALF2	R3, R2, R1	1.250	3.00	$1.91 \pm 0.8\%$	yes	I	1.02 ± 0.07	2.858 ± 0.010	0.707 ± 0.011	8.963 ± 0.8
ALF2	R3, R2	1.250	3.10	$1.90 \pm 0.0\%$	yes	I	0.79 ± 0.04	2.983 ± 0.010	0.731 ± 0.010	6.690 ± 1.0
ALF2	R3, R2	1.250	3.20	$1.74 \pm 1.0\%$	yes	I	0.69 ± 0.02	3.105 ± 0.008	0.748 ± 0.009	3.936 ± 0.9
ALF2	R3	1.3125	2.80	1.54	yes	III	5.82	2.585	0.584	14.500
ALF2	R3, R2	1.375	2.80	$1.52 \pm 5.7\%$	yes	III	5.86 ± 0.29	2.577 ± 0.000	0.573 ± 0.011	15.868 ± 0.3
ALF2	R3, R2	1.375	2.85	$1.72 \pm 3.2\%$	yes	II	3.39 ± 1.17	2.651 ± 0.009	0.600 ± 0.009	12.879 ± 0.8
ALF2	R3, R2	1.375	2.90	$1.83 \pm 1.7\%$	yes	II	2.53 ± 0.69	2.712 ± 0.018	0.633 ± 0.039	12.926 ± 0.3
ALF2	R3, R2	1.375	2.95	$1.89 \pm 0.9\%$	yes	I	1.10 ± 0.08	2.761 ± 0.007	0.649 ± 0.005	14.319 ± 0.9
ALF2	R3, R2	1.375	3.00	$1.92 \pm 0.5\%$	yes	I	0.93 ± 0.06	2.827 ± 0.005	0.668 ± 0.007	12.954 ± 0.3
ALF2	R3, R2	1.375	3.10	$1.89 \pm 0.0\%$	yes	I	0.75 ± 0.04	2.943 ± 0.002	0.686 ± 0.004	11.342 ± 0.1
ALF2	R3, R2	1.375	3.20	$1.74 \pm 1.5\%$	yes	I	0.64 ± 0.02	3.061 ± 0.001	0.700 ± 0.003	9.212 ± 0.2
ALF2	R3	1.4375	2.80	1.52	yes	III	7.37	2.549	0.540	18.960
ALF2	R3, R2, R1	1.500	2.80	$1.53 \pm 6.5\%$	yes	III	10.99 ± 3.69	2.554 ± 0.001	0.542 ± 0.006	19.203 ± 0.7
ALF2	R3, R2	1.500	2.85	$1.73 \pm 4.0\%$	yes	II	4.00 ± 0.21	2.632 ± 0.012	0.589 ± 0.001	17.356 ± 1.9
ALF2	R3, R2, R1	1.500	2.90	$1.84 \pm 1.8\%$	yes	I	1.23 ± 0.08	2.702 ± 0.004	0.625 ± 0.008	16.247 ± 0.4
ALF2	R3, R2	1.500	2.95	$1.89 \pm 1.0\%$	yes	I	0.97 ± 0.04	2.758 ± 0.003	0.634 ± 0.004	15.411 ± 0.4
ALF2	R3, R2, R1	1.500	3.00	$1.92 \pm 0.6\%$	yes	I	0.84 ± 0.03	2.817 ± 0.007	0.644 ± 0.008	14.731 ± 0.0
ALF2	R3, R2, R1	1.500	3.10	$1.87 \pm 0.5\%$	yes	I	0.69 ± 0.02	2.924 ± 0.002	0.654 ± 0.003	13.420 ± 0.2
ALF2	R3, R2	1.500	3.20	$1.73 \pm 1.9\%$	yes	I	0.58 ± 0.00	3.034 ± 0.001	0.665 ± 0.001	12.433 ± 0.5
ALF2	R3	1.5625	2.80	1.55	yes	II	4.86	2.573	0.558	18.336
ALF2	R3	1.625	2.70	1.47	no	IV				
ALF2	R3, R2	1.625	2.75	$1.43 \pm 0.8\%$	yes	III	19.21 ± 7.86	2.428 ± 0.027	0.452 ± 0.022	27.695 ± 2.6
ALF2	R3, R2	1.625	2.80	$1.52 \pm 7.2\%$	yes	II/III	4.73 ± 0.93	2.570 ± 0.010	0.553 ± 0.011	19.241 ± 1.0
ALF2	R3, R2	1.625	2.85	$1.70 \pm 7.0\%$	yes	I	1.03 ± 0.35	2.652 ± 0.011	0.582 ± 0.008	17.069 ± 0.1
ALF2	R3, R2	1.625	2.90	$1.87 \pm 2.5\%$	yes	I	1.00 ± 0.05	2.706 ± 0.005	0.610 ± 0.006	16.133 ± 0.3
ALF2	R3, R2	1.625	2.95	$1.92 \pm 1.2\%$	yes	I	0.86 ± 0.04	2.753 ± 0.008	0.609 ± 0.010	16.450 ± 0.9
ALF2	R3, R2	1.625	3.00	$1.91 \pm 0.5\%$	yes	I	0.76 ± 0.01	2.807 ± 0.005	0.615 ± 0.006	15.895 ± 0.7
ALF2	R3, R2	1.625	3.10	$1.88 \pm 0.4\%$	yes	I	0.63 ± 0.04	2.915 ± 0.007	0.626 ± 0.007	14.790 ± 0.9
ALF2	R3, R2	1.625	3.20	$1.77 \pm 1.4\%$	yes	I	0.46 ± 0.01	3.020 ± 0.005	0.633 ± 0.004	13.747 ± 0.0
ALF2	R3, R2	1.750	2.70	$1.48 \pm 0.4\%$	no	IV				
ALF2	R3, R2	1.750	2.75	$1.44 \pm 0.7\%$	yes	III	15.27 ± 4.42	2.441 ± 0.021	0.461 ± 0.009	27.672 ± 2.0
ALF2	R3, R2	1.750	2.80	$1.47 \pm 8.1\%$	yes	I	1.33 ± 0.07	2.596 ± 0.005	0.571 ± 0.005	17.814 ± 0.6
ALF2	R3, R2	1.750	2.85	$1.74 \pm 3.1\%$	yes	I	1.25 ± 0.16	2.654 ± 0.008	0.604 ± 0.029	16.516 ± 1.2
ALF2	R3, R2	1.750	2.90	$1.86 \pm 3.3\%$	yes	I	0.88 ± 0.01	2.696 ± 0.007	0.579 ± 0.007	17.401 ± 1.0
ALF2	R3, R2	1.750	2.95	$1.93 \pm 1.7\%$	yes	I	0.77 ± 0.04	2.747 ± 0.008	0.582 ± 0.010	17.381 ± 0.9
ALF2	R3, R2	1.750	3.00	$1.96 \pm 0.8\%$	yes	I	0.68 ± 0.01	2.796 ± 0.003	0.583 ± 0.005	17.260 ± 0.5
ALF2	R3, R2	1.750	3.10	$1.95 \pm 0.2\%$	yes	I	0.50 ± 0.02	2.900 ± 0.003	0.591 ± 0.004	16.533 ± 0.5

TABLE XVI. Same as Tab. XIV, but for EOS H4.

EOS	res	q	M [M_{\odot}]	ecc [10^{-2}]	BH	Type	t_{coll} [ms]	M_{BH} [M_{\odot}]	χ_{BH}	M_{disk} [$10^{-2} M_{\odot}$]
H4	R2*	1.000	2.80	1.76	?	III	14.15	2.586	0.567	11.745
H4	R3*, R2*	1.000	2.90	$1.87 \pm 0.4\%$	yes	III	6.34 ± 1.34	2.758 ± 0.004	0.666 ± 0.010	4.738 ± 0.0
H4	R3*, R2*	1.000	2.95	$1.90 \pm 0.3\%$	yes	II/III	5.29 ± 0.32	2.805 ± 0.000	0.674 ± 0.010	5.493 ± 1.2
H4	R3*, R2*	1.000	3.00	$1.88 \pm 0.1\%$	yes	II	3.70 ± 0.02	2.888 ± 0.016	0.727 ± 0.017	3.023 ± 1.2
H4	R3*, R2*	1.000	3.10	$1.81 \pm 0.2\%$	yes	I	1.36 ± 0.07	3.024 ± 0.004	0.784 ± 0.006	0.190 ± 0.1
H4	R3*, R2*	1.000	3.20	$1.62 \pm 1.0\%$	yes	I	0.91 ± 0.01	3.130 ± 0.004	0.788 ± 0.007	0.157 ± 0.0
H4	R3*, R2*	1.000	3.30	$1.40 \pm 3.8\%$	yes	I	0.77 ± 0.00	3.229 ± 0.005	0.780 ± 0.006	0.079 ± 0.0
H4	R3*, R2*	1.125	2.90	$1.87 \pm 0.4\%$	yes	III	7.83 ± 2.48	2.730 ± 0.057	0.637 ± 0.048	7.867 ± 6.2
H4	R3*, R2*	1.125	2.95	$1.88 \pm 0.3\%$	yes	III	5.17 ± 0.04	2.796 ± 0.003	0.676 ± 0.015	7.197 ± 0.8
H4	R3*, R2*	1.125	3.00	$1.88 \pm 0.2\%$	yes	II	4.09 ± 0.16	2.866 ± 0.022	0.706 ± 0.028	5.353 ± 1.5
H4	R3*, R2*	1.125	3.10	$1.80 \pm 0.3\%$	yes	I	1.17 ± 0.05	2.992 ± 0.006	0.756 ± 0.008	4.177 ± 0.0
H4	R3*, R2*	1.125	3.20	$1.59 \pm 1.1\%$	yes	I	0.89 ± 0.01	3.112 ± 0.006	0.771 ± 0.007	2.187 ± 0.2
H4	R3*, R2*	1.125	3.30	$1.39 \pm 5.4\%$	yes	I	0.76 ± 0.02	3.218 ± 0.004	0.771 ± 0.005	1.244 ± 0.1
H4	R3*, R2*	1.250	2.90	$1.89 \pm 0.5\%$	yes	III	6.28 ± 1.36	2.693 ± 0.031	0.612 ± 0.036	12.869 ± 2.8
H4	R3*, R2*	1.250	2.95	$1.90 \pm 0.3\%$	yes	III	5.14 ± 0.04	2.737 ± 0.012	0.615 ± 0.010	13.836 ± 1.2
H4	R3*, R2*	1.250	3.00	$1.87 \pm 0.1\%$	yes	II	4.17 ± 0.30	2.804 ± 0.002	0.647 ± 0.006	12.518 ± 0.4
H4	R3*, R2*	1.250	3.10	$1.78 \pm 0.3\%$	yes	I	1.10 ± 0.06	2.917 ± 0.005	0.685 ± 0.007	12.975 ± 0.0
H4	R3*, R2*	1.250	3.20	$1.55 \pm 1.2\%$	yes	I	0.86 ± 0.02	3.052 ± 0.005	0.715 ± 0.005	8.974 ± 0.2
H4	R3*, R2*	1.250	3.30	$1.36 \pm 9.0\%$	yes	I	0.74 ± 0.02	3.172 ± 0.002	0.730 ± 0.002	7.043 ± 0.3
H4	R3*, R2*	1.375	2.90	$1.90 \pm 0.3\%$	yes	III	8.96 ± 2.84	2.654 ± 0.032	0.567 ± 0.022	17.884 ± 3.1
H4	R3*, R2*	1.375	2.95	$1.90 \pm 0.2\%$	yes	III	6.93 ± 1.47	2.718 ± 0.006	0.595 ± 0.009	17.093 ± 0.1
H4	R3*, R2*	1.375	3.00	$1.88 \pm 0.0\%$	yes	II	3.04 ± 0.04	2.785 ± 0.005	0.628 ± 0.008	16.103 ± 0.1
H4	R3*, R2*	1.375	3.10	$1.76 \pm 0.7\%$	yes	I	1.02 ± 0.02	2.913 ± 0.007	0.671 ± 0.010	14.414 ± 0.3
H4	R3*, R2*	1.375	3.20	$1.50 \pm 2.1\%$	yes	I	0.82 ± 0.01	3.029 ± 0.007	0.687 ± 0.009	12.339 ± 0.5
H4	R3*, R2*	1.375	3.30	$1.30 \pm 19.1\%$	yes	I	0.67 ± 0.01	3.146 ± 0.005	0.700 ± 0.006	10.345 ± 0.5
H4	R3*, R2*	1.500	2.90	$1.90 \pm 0.3\%$	yes	III	10.97 ± 2.70	2.611 ± 0.032	0.529 ± 0.025	23.979 ± 3.4
H4	R3*, R2*	1.500	2.95	$1.90 \pm 0.2\%$	yes	I/III	1.89 ± 4.82	2.722 ± 0.043	0.610 ± 0.051	19.400 ± 3.2
H4	R3*, R2*	1.500	3.00	$1.88 \pm 0.1\%$	yes	I	1.26 ± 0.06	2.794 ± 0.009	0.633 ± 0.010	16.900 ± 0.8
H4	R3*, R2*	1.500	3.10	$1.75 \pm 1.2\%$	yes	I	0.91 ± 0.02	2.903 ± 0.006	0.647 ± 0.008	15.627 ± 0.4
H4	R3*, R2*	1.500	3.20	$1.42 \pm 2.4\%$	yes	I	0.73 ± 0.02	3.012 ± 0.006	0.655 ± 0.007	14.699 ± 0.5
H4	R3*, R2*	1.500	3.30	$1.45 \pm 52.2\%$	yes	I	0.57 ± 0.01	3.116 ± 0.000	0.660 ± 0.002	14.033 ± 0.0
H4	R2*	1.625	2.80	1.82	?	IV				
H4	R3*, R2*	1.625	2.85	$1.87 \pm 0.6\%$?	III/IV	51.79	2.492	0.446	29.693
H4	R3*, R2*	1.625	2.90	$1.90 \pm 0.1\%$	yes	I	1.81 ± 0.11	2.666 ± 0.008	0.580 ± 0.008	20.552 ± 0.5
H4	R3*, R2*	1.625	2.95	$1.90 \pm 0.1\%$	yes	I	1.31 ± 0.03	2.730 ± 0.009	0.598 ± 0.009	18.850 ± 0.3
H4	R3*, R2*	1.625	3.00	$1.87 \pm 0.6\%$	yes	I	1.10 ± 0.02	2.785 ± 0.003	0.605 ± 0.004	18.304 ± 0.1
H4	R3*, R2*	1.625	3.10	$1.71 \pm 1.9\%$	yes	I	0.79 ± 0.03	2.888 ± 0.008	0.613 ± 0.008	17.771 ± 0.7
H4	R3*, R2*	1.625	3.20	$1.35 \pm 3.0\%$	yes	I	0.57 ± 0.05	2.991 ± 0.005	0.617 ± 0.004	17.290 ± 0.3
H4	R2*	1.750	2.80	1.84	?	IV				
H4	R3*, R2*	1.750	2.85	$1.89 \pm 0.7\%$	yes	I/II	2.03 ± 0.07	2.608 ± 0.006	0.548 ± 0.006	21.656 ± 0.4
H4	R3*, R2*	1.750	2.90	$1.91 \pm 0.2\%$	yes	I	1.38 ± 0.05	2.673 ± 0.003	0.566 ± 0.003	19.938 ± 0.1
H4	R3*, R2*	1.750	2.95	$1.91 \pm 0.6\%$	yes	I	1.20 ± 0.02	2.724 ± 0.003	0.570 ± 0.004	19.712 ± 0.1
H4	R3*, R2*	1.750	3.00	$1.87 \pm 1.1\%$	yes	I	0.94 ± 0.02	2.777 ± 0.007	0.576 ± 0.007	19.309 ± 0.6
H4	R3*, R2*	1.750	3.10	$1.66 \pm 2.3\%$	yes	I	0.65 ± 0.05	2.877 ± 0.003	0.580 ± 0.003	19.156 ± 0.2